Accepted in *J. Non-Newtonian Fluid Mechanics*, September 1997

NEW CLOSURE APPROXIMATIONS FOR THE KINETIC THEORY OF FINITELY EXTENSIBLE DUMBBELLS

G. Lielens, P. Halin, I. Jaumain, R. Keunings, V. Legat
CESAME, Division of Applied Mechanics, Université catholique de Louvain, Bâtiment Euler, B-1348 Louvain-la-Neuve, Belgium

Abstract

We address the closure problem for the most elementary non-linear kinetic model of a dilute polymeric solution, known as the Warner Finitely Extensible Non-linear Elastic (FENE) dumbbell model. In view of the closure problem, the FENE theory cannot be translated into an equivalent macroscopic constitutive equation for the polymer contribution to the stress tensor. We present a general framework for developing closure approximations, based on the concept of canonical distribution subspace first introduced by Verleye and Dupret [1] in the context of fiber suspension modeling. The classical consistent pre-averaging approximation due to Peterlin (that yields the FENE-P constitutive equation) is obtained from the canonical approach as the simplest first-order closure model involving only the second moment of the configuration distribution function. A second-order closure model (referred to as FENE-P^2) is derived, which involves the second and fourth moments of the distribution function. We show that the FENE-P^2 model behaves like the FENE-P equation with a reduced extensibility parameter. In that respect, it is a close relative of the FENE-P* equation proposed by van Heel *et al.* [2]. Inspired by stochastic simulation results for the FENE theory, we propose a more sophisticated second-order closure model (referred to as FENE-L). The rheological response of the FENE-P, FENE-P^2 and FENE-L closure models are compared to that of the FENE theory in various time-dependent, one-dimensional elongational flows. Overall, the FENE-L model is found to provide the best agreement with the FENE results. In particular,

it is able to reproduce the hysteretic behaviour of the FENE model, also observed in recent experiments involving polystyrene-based Boger fluids [3], in stress versus birefringence curves during startup of flow and subsequent relaxation.

Keywords: closure approximation; constitutive equation; FENE dumbbells; kinetic theory.

1 Introduction

The continuum mechanical [4] and kinetic [5] approaches to the analysis of flowing polymers are best viewed as complementary. Ideally, one would wish to use in complex flow simulations a macroscopic constitutive equation derived from a kinetic theory model, the goal being to take account in a detailed (though coarse-grain) manner of the flow-induced configurations of the polymer molecules. Unfortunately, only the very crudest kinetic models yield equivalent macroscopic constitutive equations. With more sophisticated kinetic theories, constitutive equations can in some cases be derived using so-called closure approximations. What physics are lost in the approximation process remains for the most part an open issue, especially in complex flows. In particular, recent work [6, 7] on simple kinetic theories for dilute polymeric solutions (the FENE dumbbell model), motivated by experimental observations for Boger fluids (e.g. [3]), shows that classical closure approximations can have a significant impact on the statistical and rheological properties of the resulting model. This important observation motivates the development of micro-macro numerical techniques that use the kinetic theory model as stress calculator instead of the approximate constitutive equation, as pioneered by Laso and Öttinger with their CONNFFESSIT method [8]. Although accurate micro-macro techniques for complex flow simulations are becoming available [9-12], there is still a need for the much less compute-intensive macroscopic constitutive equations, especially in engineering design work.

In the present paper, we propose a general framework for addressing the closure problem. For illustrative purposes, we focus on the simplest non-linear kinetic theory of a dilute polymeric solution, known as the Warner Finitely Extensible Non-linear Elastic (FENE) dumbbell model [5]. The

fluid is modelled as a suspension of non-interacting dumbbells in a Newtonian solvent. Each dumbbell consists of two beads connected by a non-linear spring and it is convected by the macroscopic flow. Brownian forces, Stokes drag and the spring force contribute to the deformation and orientation of the dumbbells. In the present paper, we focus on one-dimensional transient elongational flows. Indeed, as shown by Keunings [6], a simple one-dimensional version of the FENE theory captures qualitatively and quantitatively the elongational behaviour of the actual three-dimensional theory. All theoretical developments are thus given for the one-dimensional case. Extension to three-dimensional kinematics (elongation, shear and complex flows) is documented in a companion paper [13].

With the notations of Section 4.1 of [6], the one-dimensional FENE theory is obtained by retaining only the x or xx component of all variables of interest, namely the velocity gradient $\kappa_{xx}(t) = \partial u/\partial x$, where u is the x-component of the velocity vector, the connector Q_x and the polymer stress $\tau_{p,xx}$; all other components are assumed to vanish identically. The dumbbells are thus aligned with equal probability in the positive or negative x direction, while the effect of the flow is to modify their length. The resulting mathematical problem being scalar, we shall drop all reference to the coordinate system, e.g. $\kappa = \kappa_{xx}$. In the usual dimensionless form [6, 7], the Warner non-linear spring force then reads

$$F(Q) \;=\; \frac{Q}{1 - Q^2/b}, \tag{1}$$

where b is the dimensionless finite extensibility parameter, and Q belongs to $[-\sqrt{b}, \sqrt{b}]$. The space Ψ of admissible configuration ditribution functions is therefore made of functions ψ that are even in Q, always positive and with a unit integral over the configuration space $[-\sqrt{b}, \sqrt{b}]$.

The classical Kramers' expression [5] provides the polymer contribution to the stress, i.e.

$$\tau_p = \langle Q F(Q) \rangle - 1, \tag{2}$$

where the angular brackets denote the configuration space average

$$\langle \; . \; \rangle = \int \; . \; \psi \, dQ \, . \tag{3}$$

Finally, the diffusion equation that describes the evolution of the configuration distribution function ψ reads [5]

$$\frac{D\psi}{Dt} = \frac{\partial^2}{\partial Q^2}\{\frac{1}{2}\psi\} - \frac{\partial}{\partial Q}\{\kappa(t) Q \psi\} + \frac{\partial}{\partial Q}\{\frac{1}{2} F(Q) \psi\}. \tag{4}$$

It is only in the limit of a linear Hookean spring ($b \to \infty$) that one can derive without any closure approximation a macroscopic equation for the polymer stress. The self-consistent pre-averaging approximation due to Peterlin,

$$F(Q) \;=\; \frac{Q}{1-\langle Q^2\rangle/b}, \tag{5}$$

yields the FENE-P constitutive equation [14]. It has been shown recently [6, 7] that the Peterlin approximation has a significant impact, i.e. that the FENE-P model is a poor approximation of the FENE kinetic theory, especially in transient flows. The goal of the present work is to provide a general framework within which improved closure approximations can be derived.

The paper is organized as follows. In section 2, we re-visit the stochastic simulation results obtained by Keunings [6] for a complex time-dependent elongational flow. We show that the FENE theory exhibits hysteretic behaviour in the stress versus molecular extension curve, as seen in recent experimental work with Boger fluids and in the independent theoretical work by Doyle *et al.* [3]. It is also found that the FENE-P model is not a good approximation of the FENE theory, and that it is unable to show hysteretic behaviour. These results are discussed in terms of the evolution of the FENE distribution function, which is readily available from the stochastic simulations. A general framework for addressing the closure problem is given in Section 3, inspired by the work of Verleye and Dupret [1] in the context of fiber suspension modeling. Within this framework, we derive in Section 4 first and second-order closure approximations that involve respectively the first or first two even moments of the distribution function. The first-order closure is in fact the FENE-P model. The proposed second-order FENE-P^2 model is found to behave like the FENE-P equation with a reduced extensibility parameter. Finally, the second-order FENE-L closure is proposed on the basis of the stochastic simulation results described in Section 2. In Section 5, we compare the predictions of the FENE-P, FENE-P^2 and FENE-L closure models to those of the FENE kinetic theory in several time-dependent elongational flows. Overall, the FENE-L closure is the one that provides the best agreement with the FENE theory. In particular, it is able to reproduce the hysteretic behaviour in the stress versus birefringence curves. Limitations and possible improvements of the FENE-L closure are discussed in Section 6.

2 Hysteretic behaviour

The FENE-P constitutive equation is a good approximation of the FENE theory in steady-state elongational flows. However, in time-dependent flows, the FENE and FENE-P models show significantly different dynamics of molecular extension and stress [6, 7]. Indeed, let us consider the one-dimensional complex flow kinematics defined in [6] as

$$\kappa(t) = \begin{cases} 100\, t(1-t)\exp(-4t) & \text{for } 0 \le t \le 1\,, \\ 0 & \text{otherwise}\,. \end{cases} \tag{6}$$

Figure 1 illustrates the significant impact of the Peterlin approximation on the results for the polymer stress and molecular extension [6]. We found it useful to analyze the results of Fig.1 in a different manner, namely by plotting the polymer stress versus the mean square molecular extension. The resulting curves, parameterized by the temporal variable, are shown in Fig. 2. The main result here is that the FENE kinetic theory shows hysteretic behaviour, in qualitative agreement with recent experimental data for dilute polymer solutions [3]. The FENE-P model, however, is unable to predict the hysteresis in view of the fact that Kramers' expression (2) together with the Peterlin approximation (5) yields a one-to-one relationship between stress and molecular extension. The above observations have been made independently by Doyle *et al.* [3].

Fig. 1

Further insight into the hysteretic behaviour of the FENE theory can be gained by inspection of the configuration distribution function. The latter is readily available from the stochastic simulations. As shown in Fig.2, the equilibrium distribution (specified at time $t1$) is first distorted by the velocity gradient (6) in an affine manner (eg. time $t2$). At later times (e.g. time $t3$), the longer dumbbells tend to gather close to maximum extension, thus producing a narrow peak in the distribution function; these dumbbells are essentially in an equilibrium state wherein Stokes'drag is balanced by the connector force. The shorter dumbbells, on the other hand, still experience stretching and produce a *thinning tail* in the distribution function. Finally, during the relaxation process (e.g. time $t4$), the peak-shaped distribution never spreads out again, but goes back slowly to equilibrium.

Fig. 2

Now, let us consider the fluid state at times $t3$ and $t4$, which occurs respectively during stress growth and relaxation. These two states have the

same mean square extension but quite *different distributions*. The distribution function at $t3$ is broader than at $t4$ due to the spreading effect of Stokes' drag. Consequently, the stress value, which results from the configuration average of a non-linear connector force (1) with positive concavity, is greater at $t3$ than at $t4$. More intuitively, the longer dumbbells provide the major contribution to the stress, which explains why the FENE model always shows a clockwise hysteretic cycle, when experiencing successive elongation and relaxation.

Obviously, any closure approximation which expresses the extra-stress as an algebraic function of the mean square extension alone, like the FENE-P approximation, will never be able to reproduce the hysteretic behavior. Nevertheless, one can modify the FENE-P parameters in order to bring the stress-extension curve inside the FENE hysteretic cycle. Recently, van Heel *et al.* [2] proposed a modified FENE-P model in which the parameters are determined such that important linear viscoelastic properties of the FENE theory are recovered. The resulting FENE-P* model has a reduced extensibility parameter, relative to that of the FENE theory, with the side effect of displacing the stress-extension function inside the FENE hysteresis. Although the FENE-P* model is a markedly better approximation than the FENE-P model in some flows (e.g. transient shear), it is unable to show hysteretic behaviour.

The results discussed in this section will guide us in the search for improved closure approximations of the FENE theory.

3 The closure problem: a general framework

Inspired by the work of Verleye and Dupret [1], we propose a general framework for addressing the closure problem. Although most of the theoretical developments are presented for the particular FENE dumbbell theory, the approach can be adopted for other microstructural or molecular models.

Briefly, the main idea is to describe the fluid by a finite number of state variables. Evolution equations for these state variables, derived from the diffusion equation (4), present a closure problem which is addressed with a canonical distribution subspace, i.e. a given finite-dimensional set of admissible distribution functions. The selection of state variables and canonical subspace is obviously a crucial point. Here, the insight provided by stochastic simulations is quite helpful.

3.1 State variables and evolution equations

As we wish to avoid the use of the full distribution function, we introduce a partial description of the fluid through a set X of n state variables X_i,

$$\begin{aligned} X &= \{X_1, X_2, X_3, ..., X_n\}\,, \\ &= \{A, B, C, ...\}\,. \end{aligned} \tag{7}$$

The state variables are defined as configuration space averages of given functions $f_i(Q)$ of the dumbbell configuration,

$$X_i = \langle f_i(Q) \rangle\,. \tag{8}$$

As shown in eq. 13.2-15 of [5], the state variables satisfy the following equation of change, which is readily derived from the diffusion equation (4):

$$\frac{DX_i}{Dt} = \frac{1}{2}\,\underbrace{\langle \frac{\partial^2}{\partial Q^2} f_i(Q) \rangle}_{X_i^B} + \kappa(t)\,\underbrace{\langle Q\,\frac{\partial}{\partial Q} f_i(Q) \rangle}_{X_i^D} - \frac{1}{2}\,\underbrace{\langle F(Q)\,\frac{\partial}{\partial Q} f_i(Q) \rangle}_{X_i^C}\,. \tag{9}$$

The right-hand side of (9) involves three new state variables X_i^B, X_i^D and X_i^C for the contribution of Brownian motion, hydrodynamic drag and connector force, respectively. Evolution equations can also be written for the new state variables, thus creating additional state variables, and so on. This endless procedure is well known in other fields such as turbulence and fiber suspension modeling. The closure problem then appears when we want to describe the state of the fluid only with a finite set of state variables without involving the distribution function itself. It amounts to establish a relationship between the new state variables X_i^B, X_i^D, X_i^C appearing in (9) and the original set X of state variables. In the present paper, we focus on algebraic closures.

3.2 Selection of state variables

In order to build exact or approximate closures which give good quantitative predictions, it is first necessary to select a given set of state variables. Inspired by the FENE-P model, we take the mean square extension as first state variable:

$$X_1 = \langle Q^2 \rangle\,. \tag{10}$$

In view of (2) and (9), the associated equation of change and Kramers' expression read

$$\left\{ \begin{array}{lcl} \dfrac{DX_1}{Dt} & = & 1 + 2\kappa(t)\ X_1 - \frac{1}{2}\ X_1^C\,, \\ \\ \tau_p & = & \frac{1}{2} X_1^C - 1\,. \end{array} \right. \tag{11}$$

Here, only one new state variable X_1^C appears. In the FENE-P model, Peterlin's approximation (5) provides the closure relationship between X_1^C and X_1, as discussed in Section 4.1.

For more accurate closures, we need to turn to *second-order models* involving two state variables. It would seem natural to consider X_1^C as the second state variable X_2. With such a choice for X_1 and X_2, the following evolution equations are obtained from (2) and (9):

$$\left\{ \begin{array}{lcl} \dfrac{DX_1}{Dt} & = & 1 + 2\kappa(t)\ \ X_1 - \frac{1}{2}\ X_2\,, \\ \\ \dfrac{DX_2}{Dt} & = & \frac{1}{2}\ X_2^B + \kappa(t)\ X_2^D - \frac{1}{2}\ X_2^C\,, \\ \\ \tau_p & = & \frac{1}{2} X_2 - 1\,. \end{array} \right. \tag{12}$$

Unfortunately, three new state variables X_2^B, X_2^D and X_2^C appear in the second equation. Moreover, they exhibit a complex algebraic form. This approach does not seem to be very attractive and will not be pursued in the present work.

Another possible choice that yields a second-order closure is

$$X_2 = \langle Q^4 \rangle\,. \tag{13}$$

The associated equations of change and Kramers' expression read

$$\left\{ \begin{array}{lcl} \dfrac{DX_1}{Dt} & = & 1 + 2\kappa(t)\ X_1 - \frac{1}{2}\ X_1^C\,, \\ \\ \dfrac{DX_2}{Dt} & = & 6\ X_1 + 4\kappa(t)\ X_2 - \frac{1}{2}\ X_2^C\,, \\ \\ \tau_p & = & \frac{1}{2} X_1^C - 1\,. \end{array} \right. \tag{14}$$

With this particular selection of state variables, the closure problem only arises for the connector terms X_1^C and X_2^C. This result applies more generally

to models of order n based on the n first even moments X_i of the distribution function,

$$X_i = \langle Q^{2i} \rangle \,. \tag{15}$$

The set of evolution equations then reads

$$\left\{ \begin{array}{lcl} \dfrac{DX_i}{Dt} & = & i(2i-1)\ X_{i-1} + 2i\kappa(t)\ X_i - \frac{1}{2}\ X_i^C \,, \\ \\ \tau_p & = & \frac{1}{2} X_1^C - 1 \,, \end{array} \right. \tag{16}$$

with $X_0 = 1$.

In view of the non-linearity of the connector force (1), it will in general be impossible to obtain an exact closure relationship for X_i^C. Similar difficulties would arise with more elaborate non-linear kinetic models allowing for configuration dependent drag or hydrodynamic interaction.

3.3 Canonical distribution subspaces

In order to build approximate closures, we follow the approach introduced by Verleye and Dupret [1] in the context of fiber suspension modeling. The basic idea is to restrict the space Ψ of admissible distribution functions to a so-called canonical subset Ψ^c of finite dimension m. This subspace contains all instances of a parameterized canonical distribution function ψ_p^c. The latter involves a set $p = \{\alpha, \beta, ...\}$ of m independent parameters.

In the canonical subspace, the state variables are approximated as follows:

$$\begin{array}{rcl} X_i & \approx & \langle f_i(Q) \rangle_c \,, \\ (X_i^B, X_i^D, X_i^C) & \approx & (\langle \dfrac{\partial^2}{\partial Q^2} f_i(Q) \rangle_c, \langle Q\, \dfrac{\partial}{\partial Q} f_i(Q) \rangle_c, \langle F(Q)\, \dfrac{\partial}{\partial Q} f_i(Q) \rangle_c) \,, \end{array} \tag{17}$$

where the averages $\langle \cdot \rangle_c$ are computed with the canonical distribution function ψ_p^c.

The consequence of replacing Ψ by Ψ^c is that the approximations (17) of the state variables can now be considered as functions of the set p of parameters. Using a compact notation, this property reads:

$$\begin{array}{rcl} X & \approx & \mathcal{F}(p) \,, \\ (X^B, X^D, X^C) & \approx & (\mathcal{F}^B(p), \mathcal{F}^D(p), \mathcal{F}^C(p)) \,. \end{array} \tag{18}$$

Now, assuming that $\mathcal{F}$ is invertible, it is straightforward to obtain the following approximate closure relationships:

$$(X^B, X^D, X^C) \approx (\mathcal{F}^B(\mathcal{F}^{-1}(X)), \mathcal{F}^D(\mathcal{F}^{-1}(X)), \mathcal{F}^C(\mathcal{F}^{-1}(X)))\,. \tag{19}$$

A necessary condition for $\mathcal{F}$ to be invertible is that the dimension m of the canonical subspace be equal to the number n of state variables.

The accuracy of the closure approximation (19) is governed by the selection of the canonical subspace. Indeed, the closure (19) is exact if the actual distribution function $\psi(Q)$ belongs to the canonical subspace Ψ^c; it will be a good approximation if the exact configuration distribution function stays sufficiently close to the canonical subspace during the flow process.

4 Examples of closure approximations

In the present section, we discuss several possible choices for the canonical subspace Ψ^c and the resulting closure approximations. In this paper, we focus on first and second-order closures that use the first two even moments of the distribution function as state variables (cfr Eq. (14)).

For notational convenience, let us define $X = \{A, B\}$ with

$$\begin{aligned} A &= X_1 = \langle Q^2 \rangle, & A^C &= X_1^C = 2\langle \frac{Q^2}{1 - Q^2/b} \rangle\,, \\ B &= X_2 = \langle Q^4 \rangle, & B^C &= X_2^C = 4\langle \frac{Q^4}{1 - Q^2/b} \rangle\,. \end{aligned} \tag{20}$$

It is useful to identify the set of admissible values of the pair (A, B) for the FENE fluid [15]. For a given mean square extension A in $[0, b]$, the fourth-order moment B must lie between A^2 and bA. This result is illustrated in Fig. 3. Moreover, the upper and lower bounds are reached only with particular distribution functions. The lower bound $B = A^2$ is reached for the distribution function

$$\psi(Q) = \frac{1}{2}\delta_{-\sqrt{A}}(Q) \;+\; \frac{1}{2}\delta_{\sqrt{A}}(Q)\,, \tag{21}$$

where $\delta_x(Q)$ denotes the Dirac distribution located at $Q = x$. The upper bound $B = bA$ is reached with the distribution function

$$\psi(Q) = \frac{A}{2b}\delta_{-\sqrt{b}}(Q) \;+\; (1 - \frac{A}{b})\delta_0(Q) \;+\; \frac{A}{2b}\delta_{\sqrt{b}}(Q)\,. \tag{22}$$

These results will be of particular interest in later discussions.

4.1 First-order Peterlin model (FENE-P)

As a first example, we derive the classical FENE-P model in the general framework of Section 3. We wish to develop a first-order model ($n = 1$) with the second moment A as single state variable. The canonical distribution function depends on a single parameter α ($m = 1$). Following Tanner [16], it is defined as the sum of two symmetric Dirac distributions shown in Fig. 3,

$$\psi^c_\alpha(Q) = \frac{1}{2}\delta_{-\alpha}(Q) \; + \; \frac{1}{2}\delta_\alpha(Q)\,, \tag{23}$$

with $\alpha \in [0, \sqrt{b}]$. With this particular choice of canonical subspace, the relations (18) become

$$A \;\approx\; \alpha^2\,, \qquad\qquad A^C \;\approx\; \frac{2\alpha^2}{1-\alpha^2/b}\,. \tag{24}$$

Fig. 3

Here, the inversion process is straightforward and the closure approximation (19) reads

$$A^C \approx \frac{2A}{1-A/b}\,. \tag{25}$$

This indeed is the Peterlin closure approximation (5). Finally, the evolution equation and Kramers' expression (11) yield

$$\left\{ \begin{array}{rcl} \dfrac{DA}{Dt} & = & 1 + 2\kappa(t)\; A - \dfrac{A}{1-A/b}\,, \\ \tau_p & = & \dfrac{A}{1-A/b} - 1\,, \end{array} \right. \tag{26}$$

which is the FENE-P constitutive equation.

In Fig. 3, we compare the admissible spaces for the pair (A, B) obtained with the FENE and FENE-P models. The FENE-P model yields $B = \alpha^4 = A^2$, which is the lower bound for the FENE model and is consistent with equation (21).

All first-order closures, as the FENE-P model, are characterized by the fact that the fourth moment is an algebraic expression of the second moment. This explains why those models fail to predict any hysteretic behaviour. Let us now turn to second-order closure approximations.

4.2 Second-order Peterlin model (FENE-P^2)

A first proposal for a second-order model is to select the two-parameter canonical distribution function shown in Fig. 4:

$$\psi^c_{\alpha,\beta}(Q) = \frac{\beta}{2}\delta_{-\alpha}(Q) \; + \; (1-\beta)\delta_0(Q) \; + \; \frac{\beta}{2}\delta_{\alpha}(Q)\,, \tag{27}$$

with $(\alpha,\beta) \in [0,\sqrt{b}] \times [0,1]$. With such a choice, the relations (18) become

$$\begin{array}{rclcrcl} A &\approx& \beta\alpha^2\,, & & A^C &\approx& \dfrac{2\beta\alpha^2}{1-\alpha^2/b}\,, \\ B &\approx& \beta\alpha^4\,, & & B^C &\approx& \dfrac{4\beta\alpha^4}{1-\alpha^2/b}\,. \end{array} \tag{28}$$

Fig. 4

Here again, the inversion process is rather straightforward. The evolution equation and Kramers' expression (14) yield the following second-order closure model, which we shall refer to as the FENE-P^2 equation:

$$\left\{ \begin{array}{rcl} \dfrac{DA}{Dt} &=& 1 + 2\kappa(t)\; A - \dfrac{A}{1-B/(Ab)}\,, \\ \dfrac{DB}{Dt} &=& 6A + 4\kappa(t)\; B - \dfrac{2B}{1-B/(Ab)}\,, \\ \tau_p &=& \dfrac{A}{1-B/(Ab)} - 1. \end{array} \right. \tag{29}$$

In view of the convex character of the expressions in (28), the boundary of the set of admissible values for (A,B) is the image of the corresponding boundary for (α,β). As depicted in Fig. 4, we find

$$\begin{array}{lrcl} \textbf{b1:} & \beta = 0,\; \alpha \in [0,\sqrt{b}] & \Rightarrow & B = 0,\; A = 0\,, \\ \textbf{b2:} & \alpha = \sqrt{b},\; \beta \in [0,1] & \Rightarrow & B = bA,\; A \in [0,b]\,, \\ \textbf{b3:} & \beta = 1,\; \alpha \in [0,\sqrt{b}] & \Rightarrow & B = A^2,\; A \in [0,b]\,, \\ \textbf{b4:} & \alpha = 0,\; \beta \in [0,1] & \Rightarrow & A = 0,\; B = 0\,. \end{array} \tag{30}$$

It would thus appear that the FENE and FENE-P^2 models have identical admissible spaces for the pair (A,B). This is not surprising since the FENE-P^2 canonical subspace contains the two particular distribution functions (21)

and (22) needed to reach the boundaries of the FENE admissible space of state variables. Thus, the FENE-P^2 model should be able to show hysteretic behaviour. In reality, however, for all flow processes starting from equilibrium, the FENE-P^2 state variables (A, B) never leave the thick line shown in Fig. 4, indicating degeneracy into a first-order model. This can be shown as follows. In view of (29), we have $B = 3A^2$ at equilibrium. This relation will hold at any later time since

$$\begin{aligned}
\frac{D(3A^2)}{Dt} &= 6A\frac{DA}{Dt} \\
&\overset{(29a)}{=} 6A + 12\kappa(t)\ A^2 - \frac{6A^2}{1 - B/(Ab)} \\
&= 6A + 4\kappa(t)\ B - \frac{2B}{1 - B/(Ab)} \\
&\overset{(29b)}{=} \frac{DB}{Dt}\,.
\end{aligned} \tag{31}$$

Substituting $B = 3A^2$ in (29a), we find that the FENE-P^2 model is equivalent to the first-order closure model defined as follows

$$\left\{ \begin{array}{rcl} \dfrac{DA}{Dt} &=& 1 + 2\kappa(t)\ A - \dfrac{A}{1 - A/b^*}\,, \\ \tau_p &=& \dfrac{A}{1 - A/b^*} - 1\,, \end{array} \right. \tag{32}$$

where $b^* = b/3$. Starting from an equilibrium state, the FENE-P^2 model thus behaves like a FENE-P model with a modified extensibility parameter. In that respect, it is a close relative of the FENE-P* equation proposed by van Heel *et al.* [2]. Finally, we note that the FENE-P^2 and FENE models have the same equilibrium value for the mean square extension ($A_{eq} = b/(b+3)$), while the FENE-P equation yields $A_{eq} = b/(b+1)$.

4.3 Second-order L-shaped model (FENE-L)

In order to select a better canonical subspace that would yield an improved second-order closure, it is useful to exploit the stochastic simulation results obtained for the actual FENE model [6]. In Fig. 2, one finds that the FENE

distribution function not only shows a localized peak, which would be well approximated in the FENE-P canonical subspace, but also a tail of almost uniform probability density leading approximately to a symmetric L-shape.

Inspired by these observations, we propose the following 2-parameter canonical distribution function, depicted in Fig 5:

$$\psi^c_{\alpha,\beta}(Q) = \frac{\beta}{2}\delta_{-\alpha}(Q) \; + \; \frac{(1-\beta)}{2\alpha}\left[H_{-\alpha}(Q) - H_{\alpha}(Q)\right] \; + \; \frac{\beta}{2}\delta_{\alpha}(Q), \qquad (33)$$

where $(\alpha, \beta) \in [0, \sqrt{b}] \times [0, 1]$ and $H_\alpha(Q)$ denotes the Heaviside unit step function located at $Q = \alpha$.

With this particular choice, the relations (18) become

$$\begin{aligned}
A &\approx \beta\alpha^2 + \frac{(1-\beta)\alpha^2}{3}, \\
B &\approx \beta\alpha^4 + \frac{(1-\beta)\alpha^4}{5}, \\
A^C &\approx \frac{2\beta\alpha^2}{1-\alpha^2/b} + 2(1-\beta)b\left[\frac{\sqrt{b}}{\alpha}\ln(\frac{\sqrt{b}+\alpha}{\sqrt{b}-\alpha}) - 1\right], \\
B^C &\approx \frac{4\beta\alpha^4}{1-\alpha^2/b} + 4(1-\beta)b^2\left[\frac{\sqrt{b}}{\alpha}\ln(\frac{\sqrt{b}+\alpha}{\sqrt{b}-\alpha}) - 1 - \frac{\alpha}{3\sqrt{b}}\right].
\end{aligned} \qquad (34)$$

Fig. 5

The admissible space for the pair (A, B), shown in Fig. 5, is obtained using the same method as for the FENE-P^2 canonical distribution. Its boundaries are given by

$$\begin{aligned}
&\textbf{b1:} \;\; \beta = 0,\, \alpha \in [0, \sqrt{b}] \;\; \Rightarrow \;\; B = \tfrac{9}{5}A^2,\, A \in [0, b/3]\,, \\
&\textbf{b2:} \;\; \alpha = \sqrt{b},\, \beta \in [0, 1] \;\; \Rightarrow \;\; B = \tfrac{b}{5}(6A - b),\, A \in [b/3, b]\,, \\
&\textbf{b3:} \;\; \beta = 1,\, \alpha \in [0, \sqrt{b}] \;\; \Rightarrow \;\; B = A^2,\, A \in [0, b]\,, \\
&\textbf{b4:} \;\; \alpha = 0,\, \beta \in [0, 1] \;\; \Rightarrow \;\; A = 0,\, B = 0\,.
\end{aligned} \qquad (35)$$

The FENE-L closure has a *two-dimensional* admissible space for the pair (A, B), which is the key property needed to show hysteretic behaviour. It is seen, however, to fill the admissible space of the FENE model only partially. This is due to the fact that the FENE-L canonical subspace does not include the particular distribution function (22).

Inverting the relationships (34) between (A, B) and (α, β) is not as straightforward as in the previous examples, but it remains feasible analytically. Substitution of α^2 from (34a) into (34b) yields the following quadratic equation for β:

$$20B\beta^2 + 4(5B - 9A^2)\beta + (5B - 9A^2) = 0. \tag{36}$$

For (A, B) within the admissible space, there is only one real value for β in $[0, 1]$. One thus finds

$$\begin{aligned} \beta &= \frac{(9A^2 - 5B) + \sqrt{(9A^2 - 5B)9A^2}}{10B}, \\ \alpha &= \sqrt{\frac{5B}{3A + \sqrt{9A^2 - 5B}}}. \end{aligned} \tag{37}$$

The FENE-L closure approximation is then obtained by substituting (37) in (34c) and (34d). Being rather lengthy, the resulting algebraic expressions for A^C and B^C are not detailed here and are written as $A^C(A, B)$ and $B^C(A, B)$.

Finally, the FENE-L constitutive equation is obtained from (14):

$$\left\{ \begin{aligned} \frac{DA}{Dt} &= 1 + 2\kappa(t)\ A - \tfrac{1}{2}\ A^C(A, B)\,, \\ \frac{DB}{Dt} &= 6\ A + 4\kappa(t)\ B - \tfrac{1}{2}\ B^C(A, B)\,, \\ \tau_p &= \tfrac{1}{2} A^C(A, B) - 1\,. \end{aligned} \right. \tag{38}$$

In contrast with the FENE-P and FENE-P^2 models, the FENE-L constitutive equation (38) does not prevent the state variables (A, B) from leaving their admissible space. Indeed, the following arguments reveal that nothing prevents the state variables (A, B) from crossing the boundary **b1**, while the boundaries **b2** and **b3** are impervious. With reference to (35) and Fig. 5, one finds that boundary **b2** is characterized by a non-vanishing probability of dumbbells with maximum elongation $\sqrt{b}$. This causes (A^C, B^C) to become singular, which repells (A, B) from **b2** through (38). On the other hand, the boundary **b3** is shared with the FENE model. In its vicinity, the canonical subspace Ψ^c tends to contain the actual FENE distribution, since **b3** can only be reached with the particular distribution function (21) which belongs to Ψ^c. As a result, in the vicinity of **b3**, the FENE-L closure approximation

becomes asymptotically exact and the further evolution of (A, B) will be the same as that predicted by the FENE model, i.e. crossing of **b3** is forbidden.

The situation is quite different for boundary **b1**, however, since it is not shared with the FENE model. This boundary is characterized by the disappearance of the Dirac distributions in ψ_p^c (i.e. $\beta = 0$ in (33)), and not by the fact that dumbbells have reached maximum extension. In order to prevent the pair (A, B) from crossing boundary **b1** in a general flow process, which is necessary for inverting (34), it is thus essential to add the following constraint to the FENE-L constitutive equation (38):

$$B < \frac{9}{5}A^2 \,. \tag{39}$$

Similar constraints could arise with more sophisticated closure approximations endowed with non-repelling boundaries.

5 Simulation results

In this section, we compare the predictions of the FENE-P, FENE-P^2 and FENE-L closure models to those of the FENE kinetic theory in several time-dependent one-dimensional extensional flows. In all cases, we specify $b = 50$ and the initial state is that of equilibrium. Being classical, the numerical techniques are only briefly described. Some care is however needed in the numerical implementation of the FENE-L model, as explained below.

5.1 Numerical techniques

For specified kinematics $\kappa(t)$, the behaviour of the FENE model is computed by means of the predictor-corrector stochastic simulation technique proposed by Öttinger [17], and discussed in Section 3 of [6]. We use 10^5 realizations for each stochastic simulation, which is enough to provide accurate results not only for the averages of interest (e.g $\langle Q^2 \rangle$, $\langle Q^4 \rangle$ and $\langle QF \rangle$), but also for the distribution function ψ itself. The latter is obtained directly from the stochastic simulations, in the form of normalized histograms of the dumbbell configurations [6].

The constitutive equations (26) and (29) for the FENE-P and FENE-P^2 models, respectively, are solved by means of a fifth-order Runge-Kutta technique with adaptive time stepping. For solving the constrained FENE-L

constitutive equation (38) and (39), we use a penalty method which consists in adding the following repelling force F^r to the right-hand side of (38b):

$$F^r(A,B) = K \max\left(0, B - \frac{9}{5}A^2\right)^2 , \tag{40}$$

where K is a large positive penalty factor. When numerical values for (A,B) slightly cross the boundary **b1** of the FENE-L admissible space (Fig. 5), which is inevitable with a finite penalty parameter, the connector state variables A^C and B^C are evaluated through (38) using the limiting result $B = \frac{9}{5}A^2$. Thus, the numerical implementation of FENE-L model reads

$$\left\{ \begin{array}{rcl} \dfrac{DA}{Dt} & = & 1 + 2\kappa(t)\ A - \frac{1}{2}\ A^C\left(A, \min(B, \frac{9}{5}A^2)\right) , \\ \dfrac{DB}{Dt} & = & 6\ A + 4\kappa(t)\ B - \frac{1}{2}\ B^C\left(A, \min(B, \frac{9}{5}A^2)\right) - F^r(A,B) , \\ \tau_p & = & \frac{1}{2}A^C\left(A, \min(B, \frac{9}{5}A^2)\right) - 1 . \end{array} \right. \tag{41}$$

With the above treatment of the constraint (39), the FENE-L equations (41) degenerate into the following first-order closure when the numerical values for (A,B) reach boundary **b1**:

$$\left\{ \begin{array}{rcl} \dfrac{DA}{Dt} & = & 1 + 2\kappa(t)\ A - \frac{1}{2}\ A^C\left(A, \frac{9}{5}A^2\right) , \\ \tau_p & = & \frac{1}{2}A^C\left(A, \frac{9}{5}A^2\right) - 1 . \end{array} \right. \tag{42}$$

The constraint (39) is necessary when (A,B) is close to **b1** and the growth of B is too fast with respect to the growth of A. Adding a repelling force in the evolution equation for B slows down the growth of B when necessary.

Equations (41) can be stiff, in particular when reaching boundary **b1**. They are integrated by means of a third-order Rosenbrock technique with adaptive time stepping. Convergence of numerical results has been checked by increasing the penalty factor and the accuracy demands for the adaptive time stepping.

5.2 Complex one-dimensional elongational flow

We first consider the complex transient flow defined by (6). The mean square extension and polymer stress predicted by the various models are shown in

Fig. 6.

Fig. 6

Among the three closure models discussed in the present paper, the FENE-L equation is clearly the best approximation of the FENE kinetic theory. Inspection of Fig. 6 reveals that the early FENE-P stress growth is slower than its FENE counterpart. In view of (26), this leads to a relatively faster increase of the mean square extension, which leads at later times to a strong overprediction of both extension and stress maxima. In other words, an initially-slower stress growth causes subsequent overprediction of the stress due to a faster growth of molecular extension. This phenomenon is also present for the FENE-L closure model, but it is far less pronounced. In particular, the maximum value of the polymer stress arises at about the right time and is only slightly overpredicted. The FENE-P^2 closure, on the other hand, approximates well the FENE behaviour at small times, but is quite inaccurate at later times because of the reduced maximum extension.

Fig. 7

Figure 7 shows the polymer stress as a function of mean square molecular extension. While the FENE-P and FENE-P^2 models predict a single-valued curve, the FENE-L approximation is able to show hysteretic behaviour that is qualitatively very similar to that of the FENE model. Also shown in Fig. 7 are the FENE and FENE-L distribution functions at selected values of time t_i (also defined in Fig. 6). Clearly, the FENE-L canonical subspace is able to reproduce the evolution of the FENE distribution quite satisfactorily during the entire flow process. Up to time $t2$, the essentially-Gaussian FENE distribution is approximated by a uniform FENE-L distribution (i.e. $\beta = 0$ in (33)) that is narrower, leading to a slight underprediction of the stress. The fact that no Dirac component is present in the FENE-L distribution up to time $t2$ means that the constraint (39) is active at these early stages of the flow. At time $t3$, the typical L-shape is fully developed, and FENE and FENE-L distributions are in very good agreement. During stress relaxation, e.g. at time $t4$, the L-shape subsists and agreement between the two models remains excellent. The number of dumbbells near maximum extension is low, meaning that the non-linearity of the connector force is not as important as at $t3$. Knowing the precise shape of the distribution function is thus not so crucial to compute the stress, and even a simple approximation like that of Peterlin gives good results.

Fig. 8

Further insight into the results is provided in Fig. 8 where we plot the

fourth-order moment B versus the second-order moment A. While the FENE-P and FENE-P^2 models yield a one-to-one relation, hysteretic behaviour is predicted by the FENE theory and its FENE-L approximation. We also see that the constraint (39) is active during a significant part of the FENE-L extension growth, which grinds the hysteresis curve. At later times, the FENE-L and FENE hystereses are very similar.

5.3 Startup of elongation followed by relaxation

We now consider the startup of elongation followed by relaxation. The specified velocity gradient is

$$\kappa(t) = k(H_0(t) - H_{9/k}(t)), \tag{43}$$

where k is the applied strain rate set to 2, 4 and 6 respectively. In all cases, the maximum strain is 9.

Fig. 9

First, we discuss the results for the higher strain rate ($k = 6$). In Fig. 9, we observe that the FENE-L model produces again the best approximation for both the mean square extension and the polymer stress, with the exception of the steady state values, for which the FENE-P model is slightly more accurate. The FENE-P^2 approximation is unable to predict correctly the steady-state, due to the reduced maximum elongation.

Fig. 10

The early stages of the flow are shown in Fig. 10. As in the complex flow of the previous Section and for the same reasons, the FENE-L stress growth is somewhat slower than for the FENE, while the FENE-P stress growth is slower still. The FENE-P^2 approximation, on the other hand, is slightly more accurate at the very first stages. At later times, however, it overpredicts the polymer stress, to finally diverge from FENE behavior and reach its reduced maximum extension.

Fig. 11

Figure 11 illustrates the results in terms of stress versus molecular extension. It is seen that the FENE and FENE-L models show a very similar hysteretic behaviour. Overall, the FENE-L canonical subspace is able to yield accurate approximations of the FENE distribution function. At time $t1$, however, the tail of the FENE distribution still ressembles the equilibrium Gaussian shape which cannot be approximated accurately within the FENE-L canonical subspace. The FENE-L distribution is narrower, thus leading to

the early divergence of the hysteresis curves. This is also visible in Fig. 12, where we observe that the constraint (39) is active during the early stages of the flow.

Fig. 12

The results for the smallest strain rate ($k = 2$) are shown in Fig 13. The conclusions are identical, with one noticeable exception: the FENE-L steady-state results (at $t3$) are too low and in fact less accurate than the FENE-P predictions.

Fig. 13

Although unexpected, given that the FENE-L canonical subspace contains the FENE-P canonical subspace and that we expect improved performance going from a first-order approximation to a one of second-order, this observation can be explained with the help of Fig. 14. For a moderate strain rate, the FENE-L steady state value of B does not reach the steady value of A^2, and the distribution still exhibits a tail of finite thickness which is not present in the FENE distribution. Although somewhat spread out, this FENE steady distribution is thus better approximated by a simple Dirac, i.e. within the FENE-P canonical subspace. This drawback of the FENE-L closure is less noticeable at the higher strain rate ($k = 6$) as seen by comparing the results of Fig. 11 and Fig. 14.

Fig. 14

One also observes from this comparison that the early stages (e.g. time $t1$) of the hysteresis curves are in closer agreement for the smaller strain rate. This is due to the fact that the L-shape of the distribution develops faster and that the FENE-L hysteresis curve of Fig. 15 is less grinded by the constraint (39).

Fig. 15

Finally, we compare in Fig. 16 the FENE and FENE-L hystereses for various strain rates. The qualitative agreement is excellent. Quantitatively, the FENE-L closure suffers somewhat from two drawbacks: underprediction of the stress at the early stages, especially for high strain rates, and underprediction of the steady-state molecular extension and stress, especially for small strain rates. Ways to eliminate these drawbacks are given in the Section 6.

Fig. 16

5.4 Periodic flow

Finally, we consider the periodic flow kinematics given by

$$\kappa(t) = 4abs(sin(t)). \tag{44}$$

In contrast with the previous flow problems, the fluid experiences an ever-increasing strain (Fig. 17). Even though the strain rate vanishes periodically, the molecular configurations do not recover the initial equilibrium distribution, due to memory effects. Indeed, we shall see that the present problem is even better solved by the FENE-P closure than by the FENE-L model once a periodic rheological response is reached.

Fig. 17

Inspection of Fig. 17 reveals that the results obtained for the first period of $\kappa(t)$ are very similar to those of the previous sections; the FENE-L closure performs very well indeed. The picture is a bit different for the second and third cycles, where a periodic regime is reached. Here, the FENE-P results are virtually exact, while the FENE-L closure somewhat underpredicts the stress and molecular extension. Not surprisingly, the FENE-P^2 approximation is quite inaccurate after the early stages of the first cycle, again due to its reduced extensibility parameter.

Fig. 18

Insight into the behaviour of the FENE-L closure in the periodic regime can be gained from Fig. 18. The FENE theory settles to a very thin limit cycle in the stress-molecular extension plane, that is indeed very well approximated by the FENE-P single-valued curve. While the FENE-L closure accurately captures the first cycle of the periodic flow (up to time $t2$), it then reaches a wider limit cycle. The main point here is that at time $t2$, which corresponds to a minimum in molecular extension and is the starting point of the second cycle, the FENE distribution is *not* that of equilibrium. It is rather a somewhat localised peak whose width and location vary at later times in a periodic manner (cfr. results at $t3$ and $t4$). This behaviour is very well captured by the simple Dirac functions of the FENE-P canonical subspace. The more sophisticated FENE-L distributions perform overall quite satisfactorily, but not as well. Between $t2$ and $t3$, the FENE distribution is displaced towards higher dumbbell lengths and develops a small tail which does not, however, extend back to the origin of the Q-axis. The FENE-L model captures this behaviour, but of course with a uniform tail,

which has the effect of displacing the Dirac distribution slightly too far in the direction of higher dumbbell lengths. The net result is that the stress is somewhat overpredicted, which explains the divergence of the FENE and FENE-L limit cycles between $t2$ and $t3$ (Fig. 18). Finally, at time $t4$, a slight "parasitic" tail remains in the FENE-L distribution, as in the examples of Section 5.3, with the same effect of slightly underpredicting the maximum in stress and molecular extension.

Fig. 19

Figure 19 confirms that, once in the periodic regime, the FENE behaviour degenerates into that of the FENE-P closure. Indeed, the limit cycle is very thin and lies close to the diagonal boundary of the diagram, which precisely contains the FENE-P response. Overall, the FENE-L closure behaves very well, but it predicts a limit cycle that is a bit too thick.

6 Discussion

It is clear from the results of the previous section that the FENE-L model is overall the best available closure approximation of the FENE kinetic theory. Its behaviour in three-dimensional flow kinematics (elongation and shear) is also quite good, as documented in a companion paper [13]. Improvements of the FENE-L closure are of course possible. In this section, we make a few proposals that alleviate the limitations of the FENE-L closure, at the expense of much higher numerical complexity.

As seen in Section 5.3, the first drawback to eliminate is the presence of a "parasitic" tail which somewhat perturbs the steady-state elongation results. This problem arises because a Dirac distribution function alone is too narrow to satisfy steady-state for both A and B. A natural solution is to use a broader distribution to represent the peak at the end of the tail, for example a rectangle starting at $Q = \alpha$ and of width $w(\alpha)$. The width function $w(\alpha)$ may be selected such that there always exists a value of α which satisfies equilibrium for A and B under any rate of steady elongation. This function will of course depend on the extensibility parameter b, which implies that the canonical subspace depends on this parameter:

$$\psi^c_{\alpha,\beta}(Q) = \frac{\beta}{2} P_{-\alpha}(Q) + \frac{1-\beta}{2\alpha} \left[H_{-\alpha}(Q) - H_{\alpha}(Q) \right] + \frac{\beta}{2} P_{\alpha}(Q) \qquad (45)$$

$$\text{with} \left\{ \begin{array}{rcll} P_x(Q) & = & \left[H_x(Q) - H_{x+w(x)}(Q)\right]/w(x) & \text{for } x > 0 \\ P_x(Q) & = & \left[H_{x-w(-x)}(Q) - H_x(Q)\right]/w(-x) & \text{for } x < 0 \end{array} \right. \quad (46)$$

With this more sophisticated canonical subspace, but still of second order, the "parasitic" tail disappears at steady state.

The second drawback of the FENE-L closure, maybe less important, is the underprediction of the polymer stress in the early stages of rapid elongation, starting from equilibrium. The problem arises because the FENE distribution as a tail of Gaussian shape there, before becoming more or less uniform at later times. The solution to this problem is of course to take this shape into account in the canonical subspace, e.g. with a tail close to a Gaussian distribution when the peak is low, and ever more uniform as the peak grows. This is achieved in a natural way with the following canonical distribution function:

$$\psi^c_{\alpha,\beta}(Q) = h(\alpha,\beta)\delta_{-\alpha}(Q) + \mathrm{G}_\beta(Q)\left[H_{-\alpha}(Q) - H_\alpha(Q)\right] + h(\alpha,\beta)\delta_\alpha(Q) \quad (47)$$

where $\mathrm{G}_\beta(Q)$ denotes a Gaussian distribution with mean 0 and variance β variance, and $h(\alpha,\beta) = \int_\alpha^\infty G_\beta(Q)dQ$.

Fig. 20

Combining (45) and (47), we obtain the following canonical distribution function

$$\psi^c_{\alpha,\beta}(Q) = h(\alpha,\beta)P_{-\alpha}(Q) + \mathrm{G}_\beta(Q)\left[H_{-\alpha}(Q) - H_\alpha(Q)\right] + h(\alpha,\beta)P_\alpha(Q)\,, \quad (48)$$

which is shown in Fig. 20 for different values of the parameters α and β. Obviously, the resulting canonical subspace is even more capable of an accurate description of FENE behaviour than that of FENE-L, without being of higher dimension. The price to pay, however, is that the new closure cannot be derived analytically as the FENE-L is, since the integrals and inversion processes involved must be performed numerically.

One problem where the FENE-L closure is slightly inaccurate, and which is not adressed by any 2-parameter canonical distribution, is the startup of elongation from non-equilibrium conditions (cfr Section 5.4). In fact, a second order model will never solve this problem since it cannot distinguish a distribution with a long and thin tail from one with a short and thick tail. This effect can be seen as a weak second-order hysteresis, where two different distributions share the same second and fourth-order moments, but yield slightly different polymer stresses.

Although the general framework presented in Section 3 would allow the development of third or higher-order closure approximations, we feel that the resulting numerical complexity is not worth it. Moreover, only two output state variables are really relevant, namely A^C which is used to calculate the polymer stress, and the second moment A, which is the most basic description of the polymer configurations. Those quantities can be compared with experimental data from rheometry and birefringence techniques, respectively. A second-order model thus appears to be a good compromise between accuracy and complexity.

7 Conclusions

We have proposed a general framework for deriving closure approximations for non-linear kinetic theories. Within this framework, the proposed FENE-L approximation of the FENE dumbbell kinetic theory is shown to behave very well in various one-dimensional, transient elongational flows. In particular, it is able to show hysteretic behaviour in flows involving growth and subsequent relaxation, which is out of reach for a first-order closure approximation such as the FENE-P or FENE-P* models. Extension of the FENE-L closure to three-dimensional flow kinematics is documented in [13]. Stochastic simulation of the underlying model (here, the FENE theory) is the key to the appropriate selection of canonical subspace. It is also a practical tool for testing the performance of new closure approximations. Finally, we wish to argue that the development of ever more accurate and thus increasingly complex closure approximations is not useful if pursued too far. In that respect, the FENE-L closure appears to offer a good compromise between accuracy and complexity.

Acknowledgments

The work of G. Lielens is supported by the COST 512 European Project, locally financed by the Government of the Walloon Region, Belgium. The work of I. Jaumain is supported by the BRITE/EURAM project MPFLOW CT96-145. The work of V. Legat is supported by the Belgian *Fonds National de la Recherche Scientifique* (FNRS).

References

[1] V. Verleye and F. Dupret. Prediction of fibre orientation in complex injection moulded parts. In C.E. Altan D.A. Siginer, W.E. Van Arsdale and A.N. Alexandrou, Editors, *Developments in Non-Newtonian Flows*, pages 139–163. AMD-Vol.175 (ASME, New York), 1993.

[2] A.P.G. van Heel, M.A. Hulsen, and B.H.A.A van den Brule. On the selection of parameters in the FENE-P model. *J. Non-Newtonian Fluid Mech.*, submitted 1997.

[3] P.S. Doyle, E.S.G. Shaqfeh, G.H. McKinley, and S.H. Spiegelberg. Relaxation of dilute polymer solutions following extensional flow. *J. Non-Newtonian Fluid Mech.*, submitted 1997.

[4] R.B. Bird, R.C. Armstrong, and O. Hassager. *Dynamics of Polymeric Liquids, Vol.1, Fluid mechanics.* Wiley-Interscience, New York, 2nd edition 1987.

[5] R.B. Bird, C.F. Curtiss, R.C. Armstrong, and O. Hassager. *Dynamics of Polymeric Liquids, Vol.2, Kinetic theory.* Wiley-Interscience, New York, 2nd edition 1987.

[6] R. Keunings. On the Peterlin approximation for finitely extensible dumbbells. *J. Non-Newtonian Fluid Mech.*, 68:85–100, 1997.

[7] M. Herrchen and H.C. Öttinger. A detailed comparison of various FENE dumbbell models. *J. Non-Newtonian Fluid Mech.*, 68:17–42, 1997.

[8] M. Laso and H.C. Öttinger. Calculation of viscoelastic flow using molecular models: the CONNFFESSIT approach. *J. Non-Newtonian Fluid Mech.*, 47:1–20, 1993.

[9] K. Feigl, M. Laso, and H.C. Öttinger. The CONNFFESSIT approach for solving a two-dimensional viscoelastic fluid problem. *Macromolecules*, 28:3261–3274, 1995.

[10] M.A. Hulsen, A.P.G. van Heel, and B.H.A.A. van den Brule. Simulation of viscoelastic flows using Brownian configuration fields. *J. Non-Newtonian Fluid Mech.*, 70:79–101, 1997.

[11] C.C. Hua and J.D. Schieber. Application of kinetic theory models in spatiotemporal flows for polymer solutions, liquid crystals and polymer melts using the CONNFFESSIT approach. *Chem. Eng. Sci.*, 51:1473–1485, 1996.

[12] R. Keunings and P. Halin. Macroscopic and mesoscale approaches to the computer simulation of viscoelastic flows. In J.R.A. Pearson, M.J. Adams, R.A. Mashelkar and A.R. Rennie, Editors, *Dynamics of Complex Fluids*. Imperial College Press - The Royal Society, in press 1997.

[13] G. Lielens, R. Keunings, and V. Legat. Evaluation of the FENE-L model in three-dimensional flow fields, in preparation.

[14] R.B. Bird, P.J. Dotson, and N.L. Johnson. Polymer solution rheology based on a finitely extensible bead-spring chain model. *J. Non-Newtonian Fluid Mech.*, 7:213–235, 1980.

[15] G. Lielens. PhD thesis, Université catholique de Louvain, Belgium, in preparation.

[16] R.I. Tanner. Stresses in dilute solutions of bead-nonlinear-spring macromolecules. II. Unsteady flows and approximate constitutive relations. *Trans. Soc. Rheol.*, 19:37–65, 1975.

[17] H.C. Öttinger. *Stochastic Processes in Polymeric Fluids: Tools and Examples for Developing Simulation Algorithms*. Springer, Berlin, 1996.

8 Captions for figures

Figure 1: One-dimensional complex flow: evolution of strain rate and strain. Comparison between FENE (thick curves) and FENE-P (dashed curves) results for the polymer stress and mean square extension ($b = 50$).

Figure 2: One-dimensional complex flow: polymer stress versus mean square extension ($b = 50$). Comparison between FENE (thick curve) and FENE-P (dashed curve) results. FENE distribution function at discrete values of time, also defined in Fig. 1.

Figure 3: FENE-P canonical distribution function and admissible spaces for the second and fourth moments. Gray area: FENE theory; lower boundary (thick line): FENE-P approximation.

Figure 4: FENE-P^2 canonical distribution function. Admissible spaces for the second and fourth moments. Gray area: FENE theory and FENE-P^2 approximation; thick line: FENE-P^2 approximation for flow processes starting from equilibrium.

Figure 5: FENE-L canonical distribution function and admissible spaces for the second and fourth moments. Dark and light gray areas: FENE theory; dark gray area: FENE-L approximation. The symbol $\circ$ marks the junction between boundaries **b1** and **b2** of the FENE-L admissible space.

Figure 6: One-dimensional complex flow: evolution of strain rate and strain. Comparison between FENE-P, FENE-P^2, FENE-L and FENE results for the polymer stress and mean square extension ($b = 50$). Upper dashed curve: FENE-P; lower dashed curve: FENE-P^2; thin curve: FENE-L; thick curve: FENE.

Figure 7: One-dimensional complex flow: polymer stress versus mean square extension ($b = 50$). Dashed curve (left): FENE-P^2; dashed curve (right): FENE-P; thin curve: FENE-L; thick curve: FENE. Comparison between FENE and FENE-L distribution functions at four selected times, also defined in Fig. 6. The symbols $\diamond$ and $\circ$ mark these times on the FENE-L and FENE hystereses, respectively.

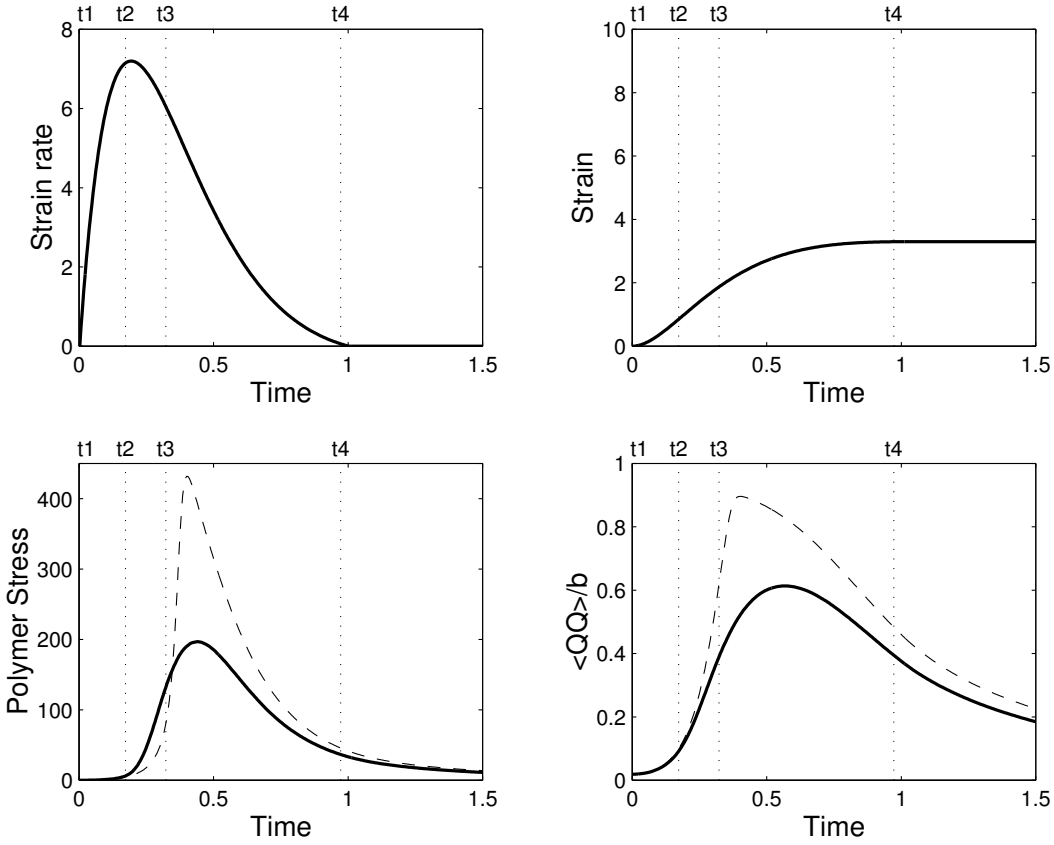

Figure 1: One-dimensional complex flow: evolution of strain rate and strain. Comparison between FENE (thick curves) and FENE-P (dashed curves) results for the polymer stress and mean square extension ($b = 50$).

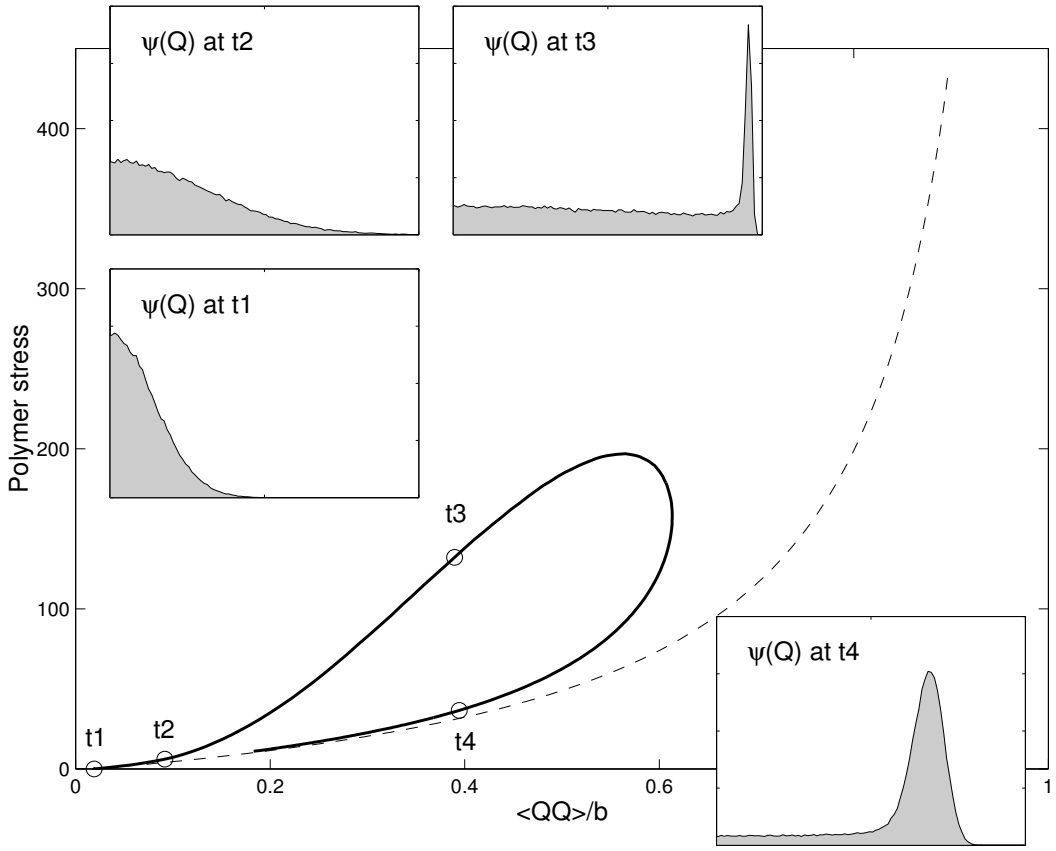

Figure 2: One-dimensional complex flow: polymer stress versus mean square extension ($b = 50$). Comparison between FENE (thick curve) and FENE-P (dashed curve) results. FENE distribution function at discrete values of time, also defined in Fig. 1.

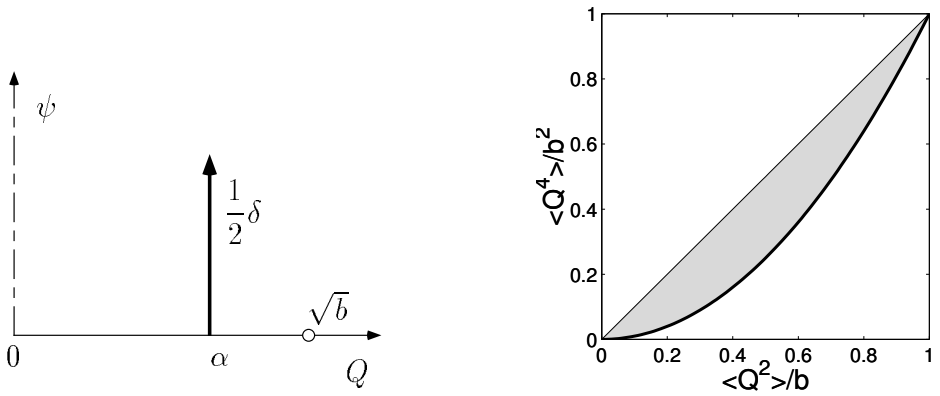

Figure 3: FENE-P canonical distribution function and admissible spaces for the second and fourth moments. Gray area: FENE theory; lower boundary (thick line): FENE-P approximation.

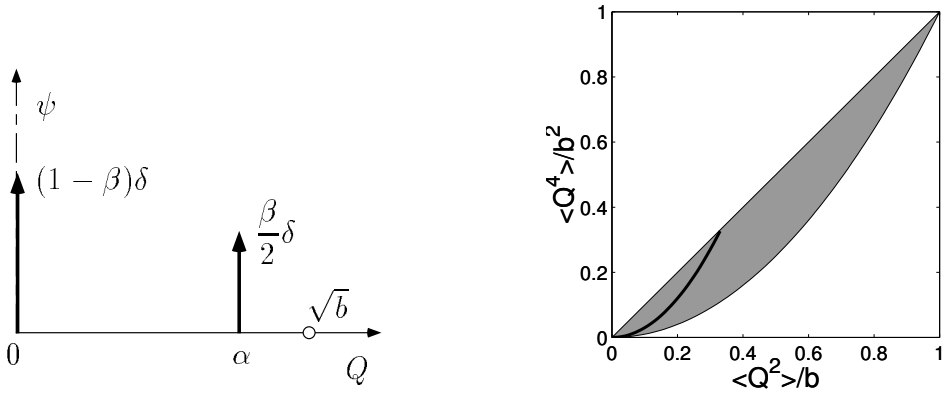

Figure 4: FENE-P^2 canonical distribution function and admissible spaces for the second and fourth moments. Gray area: FENE theory and FENE-P^2 approximation; thick line: FENE-P^2 approximation for flow processes starting from equilibrium.

Figure 8: One-dimensional complex flow: evolution of fourth moment versus second moment for FENE-P, FENE-P^2, FENE-L and FENE models (thick curves) with their admissible space (gray areas). The symbol $\circ$ marks the junction between boundaries **b1** and **b2** of the FENE-L admissible space. The FENE and FENE-L hysteresis are travelled clockwise.

Figure 9: Startup of elongation followed by relaxation: evolution of strain rate and strain. Comparison between FENE-P, FENE-P^2, FENE-L and FENE results for the polymer stress and mean square extension ($b = 50$ and $k = 6$). Upper dashed curve: FENE-P; lower dashed curve: FENE-P^2; thin curve: FENE-L; thick curve: FENE.

Figure 10: Results of Fig. 9 at the early stages of elongation. Upper dashed curve: FENE-P; lower dashed curve: FENE-P^2; thin curve: FENE-L; thick curve: FENE.

Figure 11: Startup of elongation followed by relaxation: polymer stress versus mean square extension ($b = 50$ and $k = 6$). Dashed curve (left): FENE-P^2; dashed curve (right): FENE-P; thin curve: FENE-L; thick curve: FENE. Comparison between FENE and FENE-L distribution functions at four selected times, also defined in Fig. 9. The symbols $\diamond$ and $\circ$ mark these times on the FENE-L and FENE hystereses, respectively.

Figure 12: Startup of elongation followed by relaxation ($b = 50$ and $k = 6$): evolution of fourth moment versus second moment for FENE-P, FENE-P^2, FENE-L and FENE models (thick curves) with their admissible space (gray areas). The symbol $\circ$ marks the junction between boundaries **b1** and **b2** of the FENE-L admissible space. The FENE and FENE-L hystereses are travelled clockwise.

Figure 13: Startup of elongation followed by relaxation ($b = 50$ and $k = 2$): evolution of strain rate and strain. Comparison between FENE-P, FENE-P^2, FENE-L and FENE results for the polymer stress and mean square extension. Upper dashed curve: FENE-P; lower dashed curve: FENE-P^2; thin curve: FENE-L; thick curve: FENE.

Figure 14: Startup of elongation followed by relaxation: polymer stress versus mean square extension ($b = 50$ and $k = 2$). Dashed curve (left):

FENE-P^2; dashed curve (right): FENE-P; thin curve: FENE-L; thick curve: FENE. Comparison between FENE and FENE-L distribution functions at four selected times, also defined in Fig. 13. The symbols $\diamond$ and $\circ$ mark these times on the FENE-L and FENE hystereses, respectively.

Figure 15: Startup of elongation followed by relaxation ($b = 50$ and $k = 2$): evolution of fourth moment versus second moment for FENE-P, FENE-P^2, FENE-L and FENE models (thick curves) with their admissible space (gray areas). The symbol $\circ$ marks the junction between boundaries **b1** and **b2** of the FENE-L admissible space. The FENE and FENE-L hystereses are travelled clockwise.

Figure 16: Startup of elongation followed by relaxation for different strain rates ($k = 2$, 4 and 6): polymer stress versus mean square extension ($b = 50$). Comparison between FENE (left) and FENE-L (right).

Figure 17: Periodic flow: evolution of strain rate and strain. Comparison between FENE-P, FENE-P^2, FENE-L and FENE results for the polymer stress and mean square extension ($b = 50$). Upper dashed curve: FENE-P; lower dashed curve: FENE-P^2; thin curve: FENE-L; thick curve: FENE.

Figure 18: Periodic flow : polymer stress versus mean square extension ($b = 50$). Dashed curve (left): FENE-P^2; dashed curve (right): FENE-P; thin curve: FENE-L; thick curve: FENE. Comparison between FENE and FENE-L distribution functions at four selected times, also defined in Fig. 17. The symbols $\diamond$ and $\circ$ mark these times on the FENE-L and FENE hystereses, respectively.

Figure 19: Periodic flow: evolution of fourth moment versus second moment for FENE-P, FENE-P^2, FENE-L and FENE models (thick curves) with their admissible space (gray areas). The symbol $\circ$ marks the junction between boundaries **b1** and **b2** of the FENE-L admissible space. The FENE and FENE-L hystereses are travelled clockwise.

Figure 20: Proposal for an improved second-order closure: canonical distribution function (48) for different values of the parameters α and β ($\alpha_1 > \alpha_2$, $\beta_1 < \beta_2 < \beta_3$).

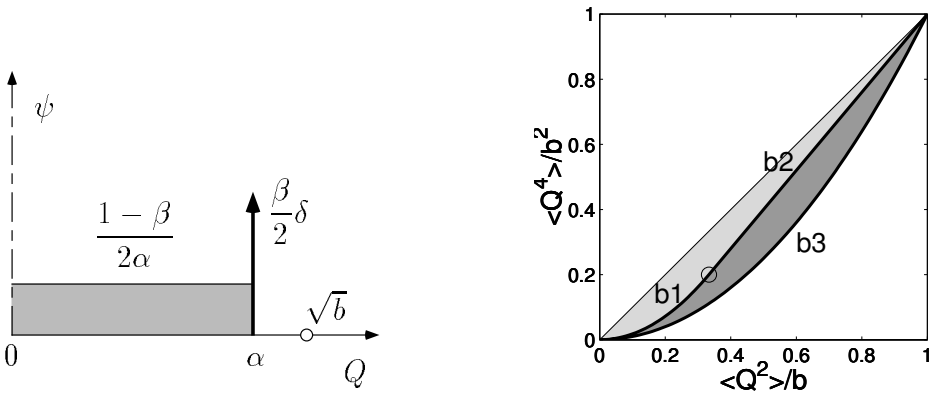

Figure 5: FENE-L canonical distribution function and admissible spaces for the second and fourth moments. Dark and light gray areas: FENE theory; dark gray area: FENE-L approximation. The symbol ∘ marks the junction between boundaries **b1** and **b2** of the FENE-L admissible space.

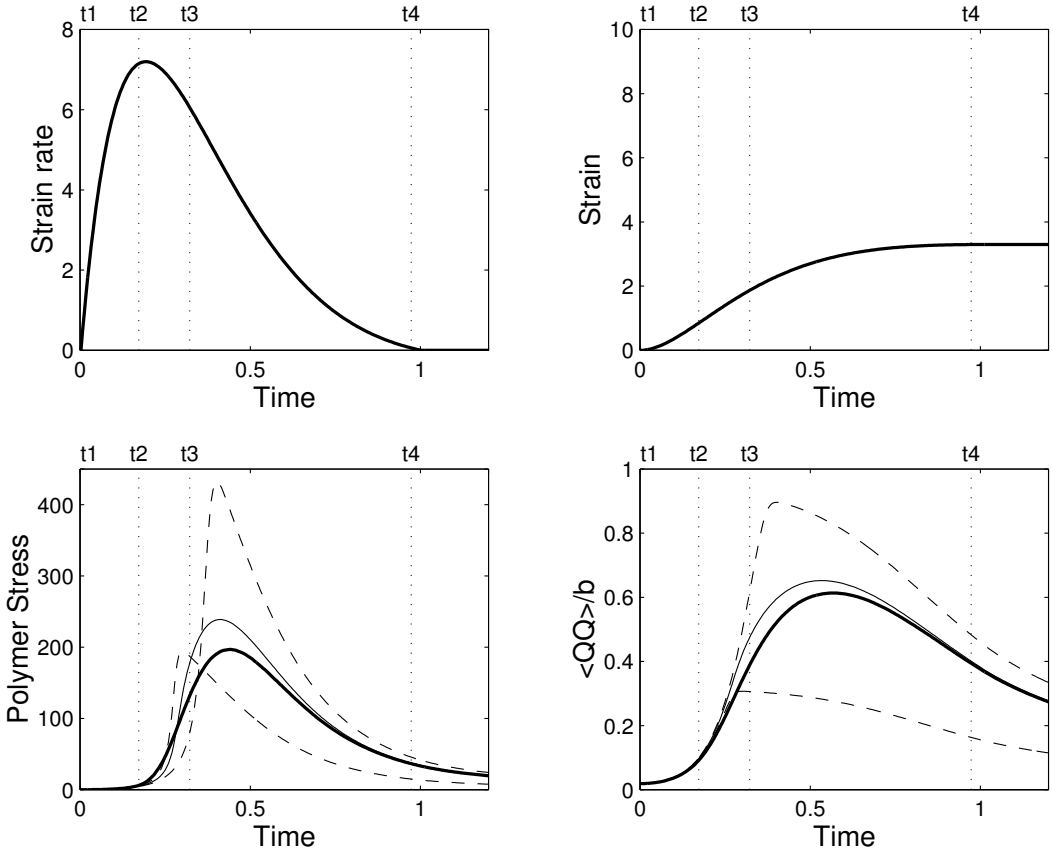

Figure 6: One-dimensional complex flow: evolution of strain rate and strain. Comparison between FENE-P, FENE-P^2, FENE-L and FENE results for the polymer stress and mean square extension ($b = 50$). Upper dashed curve: FENE-P; lower dashed curve: FENE-P^2; thin curve: FENE-L; thick curve: FENE.

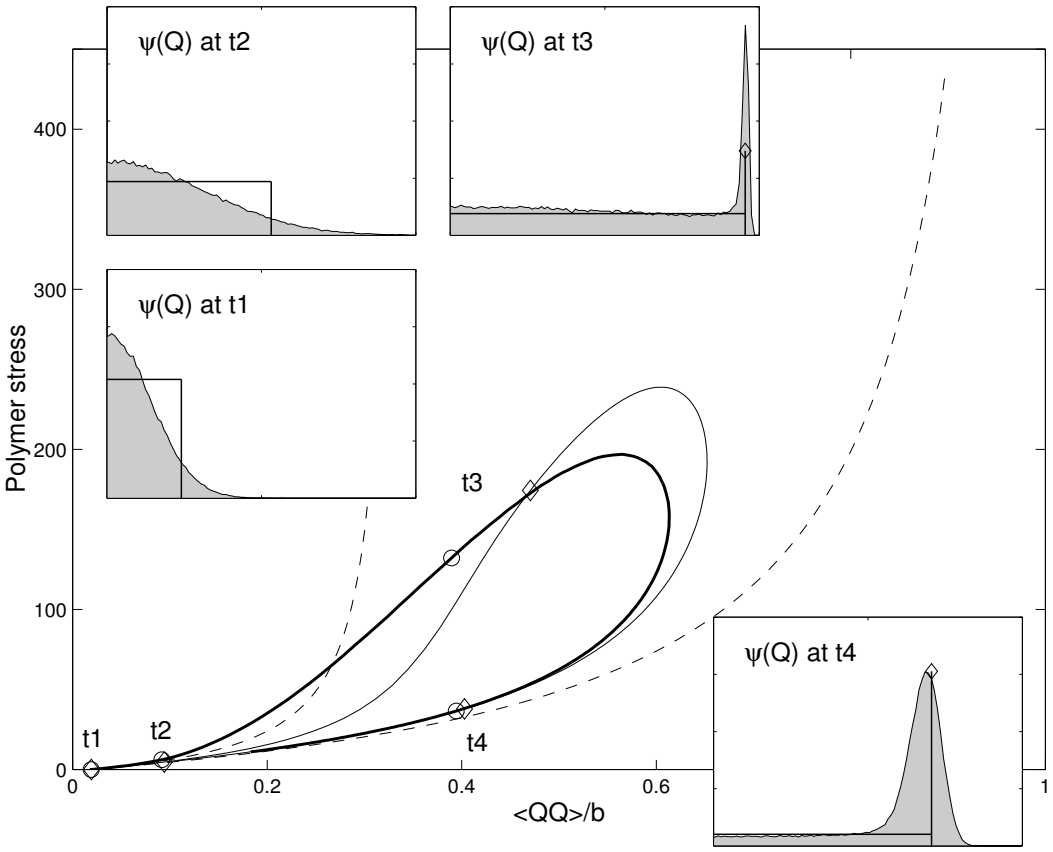

Figure 7: One-dimensional complex flow: polymer stress versus mean square extension ($b = 50$). Dashed curve (left): FENE-P^2; dashed curve (right): FENE-P; thin curve: FENE-L; thick curve: FENE. Comparison between FENE and FENE-L distribution functions at four selected times, also defined in Fig. 6. The symbols $\diamond$ and $\circ$ mark these times on the FENE-L and FENE hystereses, respectively.

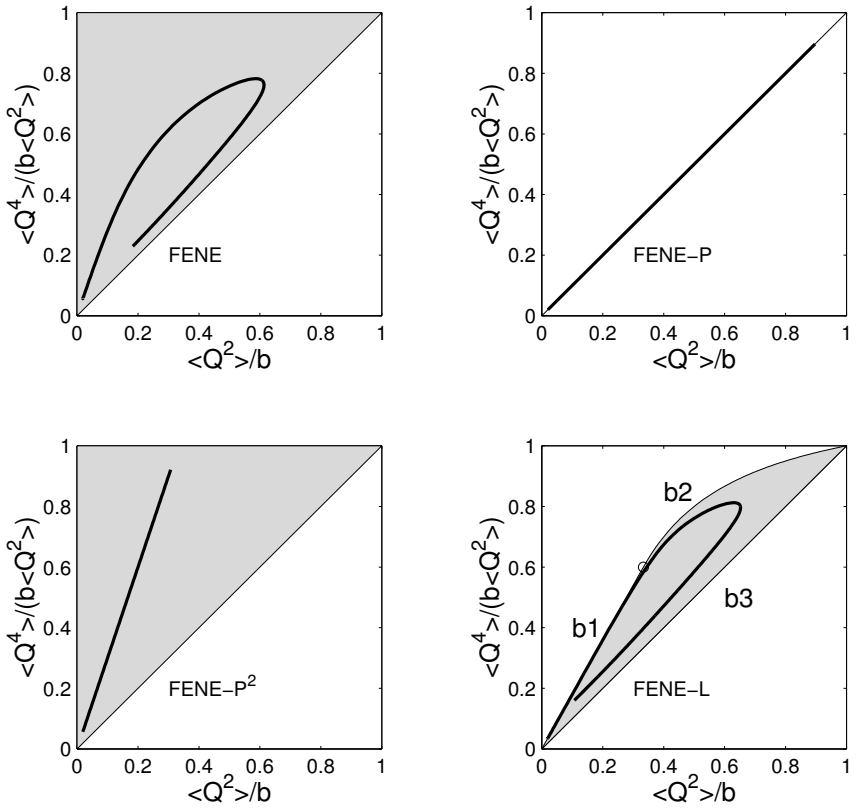

Figure 8: One-dimensional complex flow ($b = 50$): evolution of fourth moment versus second moment for FENE-P, FENE-P^2, FENE-L and FENE models (thick curves) with their admissible space (gray areas). The symbol $\circ$ marks the junction between boundaries **b1** and **b2** of the FENE-L admissible space. The FENE and FENE-L hystereses are travelled clockwise.

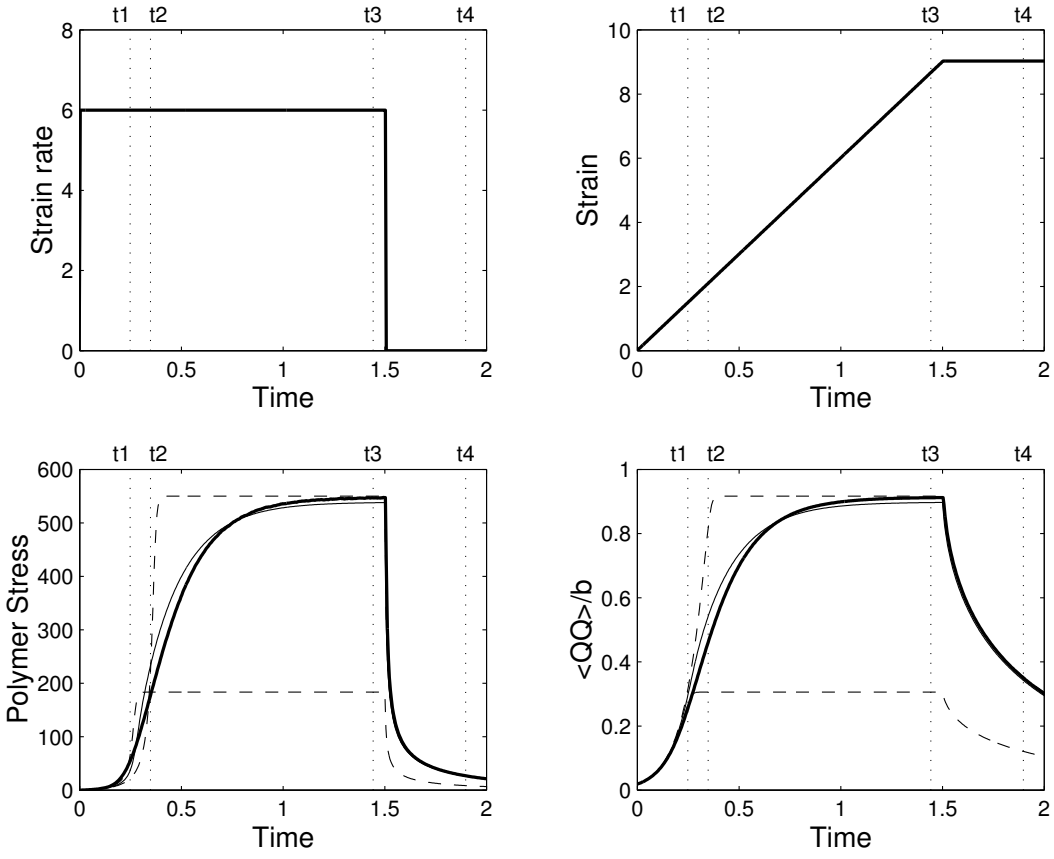

Figure 9: Startup of elongation followed by relaxation: evolution of strain rate and strain. Comparison between FENE-P, FENE-P^2, FENE-L and FENE results for the polymer stress and mean square extension ($b = 50$ and $k = 6$). Upper dashed curve: FENE-P; lower dashed curve: FENE-P^2; thin curve: FENE-L; thick curve: FENE.

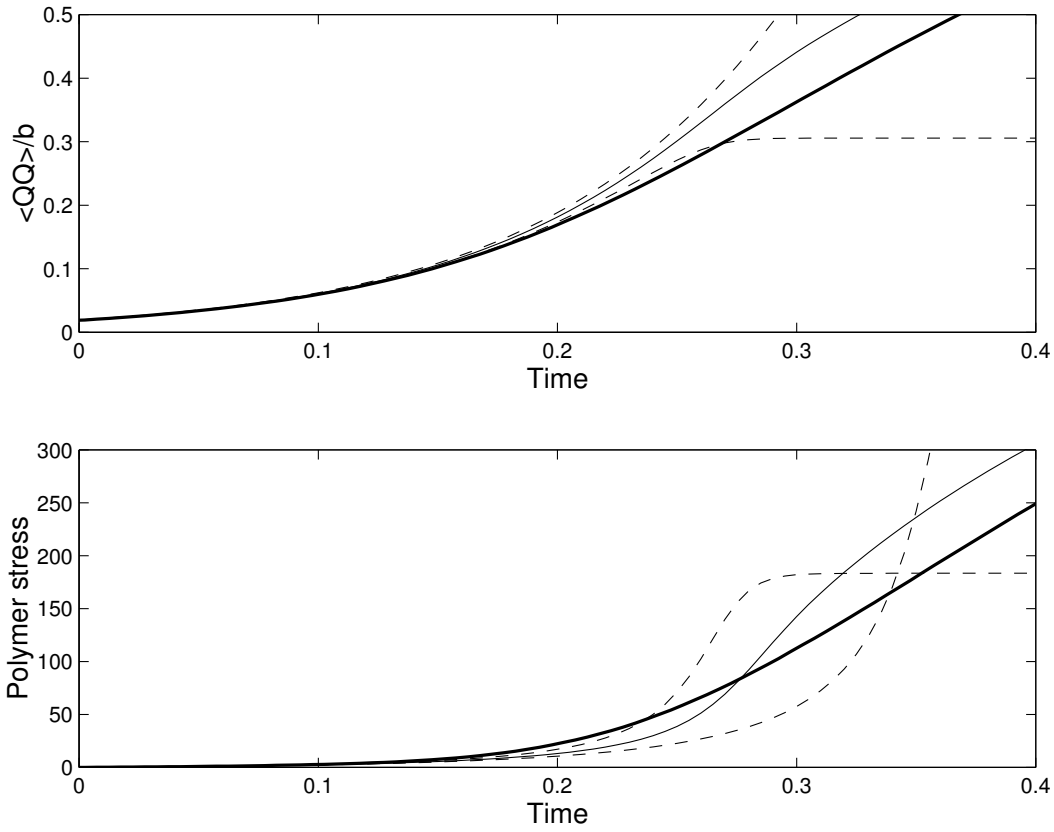

Figure 10: Results of Fig. 9 at the early stages of elongation. Upper dashed curve: FENE-P; lower dashed curve: FENE-P^2; thin curve: FENE-L; thick curve: FENE.

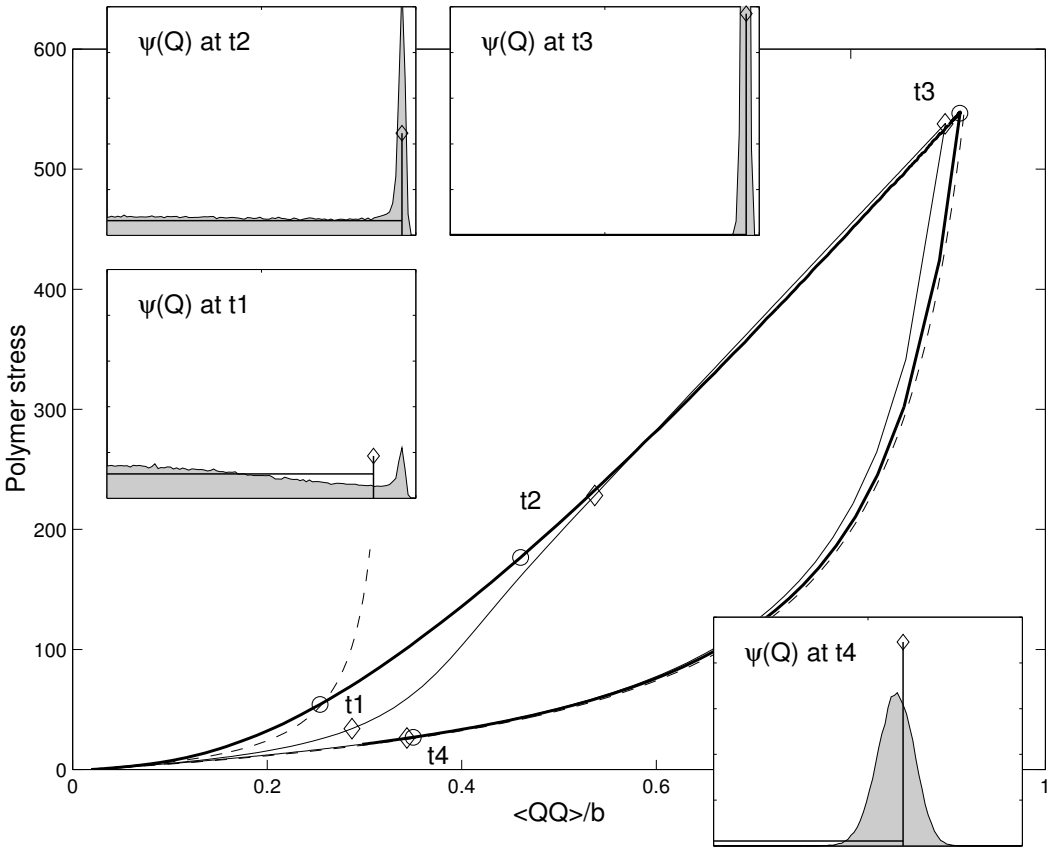

Figure 11: Startup of elongation followed by relaxation: polymer stress versus mean square extension ($b = 50$ and $k = 6$). Dashed curve (left): FENE-P^2; dashed curve (right): FENE-P; thin curve: FENE-L; thick curve: FENE. Comparison between FENE and FENE-L distribution functions at four selected times, also defined in Fig. 9. The symbols $\diamond$ and $\circ$ mark these times on the FENE-L and FENE hystereses, respectively.

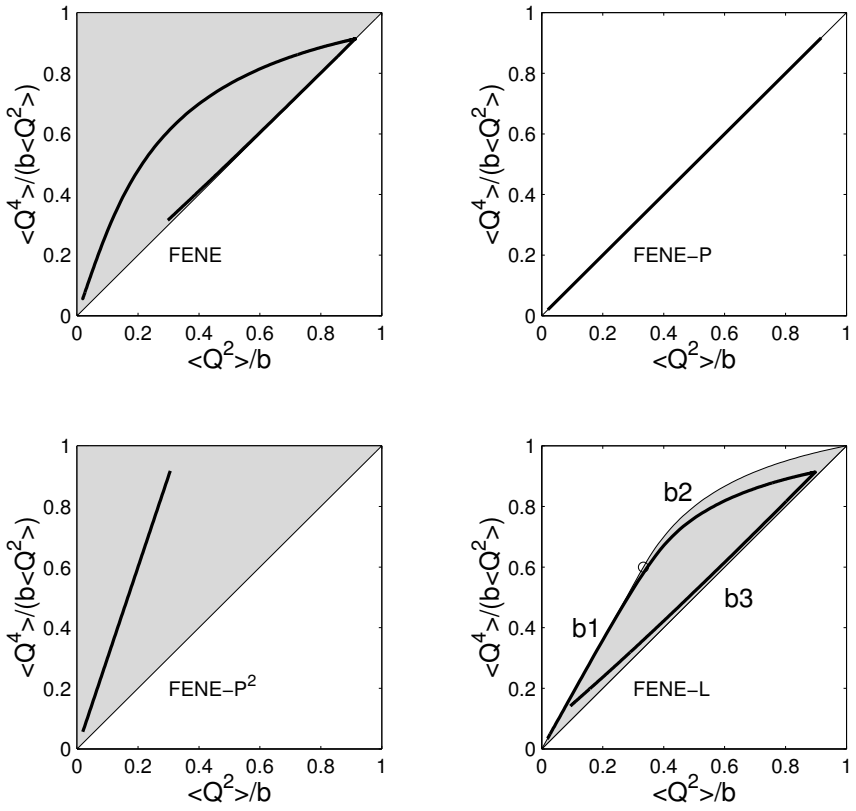

Figure 12: Startup of elongation followed by relaxation ($b = 50$ and $k = 6$): evolution of fourth moment versus second moment for FENE-P, FENE-P^2, FENE-L and FENE models (thick curves) with their admissible space (gray areas). The symbol ∘ marks the junction between boundaries **b1** and **b2** of the FENE-L admissible space. The FENE and FENE-L hystereses are travelled clockwise.

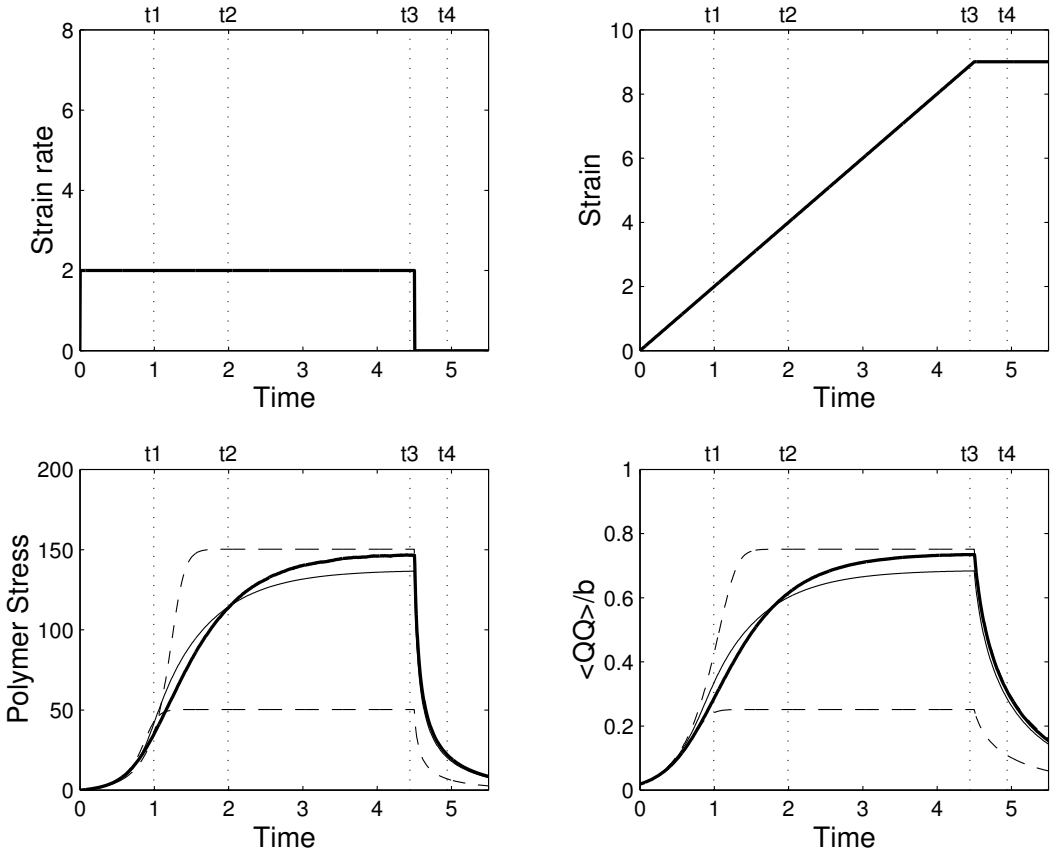

Figure 13: Startup of elongation followed by relaxation ($b = 50$ and $k = 2$): evolution of strain rate and strain. Comparison between FENE-P, FENE-P^2, FENE-L and FENE results for the polymer stress and mean square extension. Upper dashed curve: FENE-P; lower dashed curve: FENE-P^2; thin curve: FENE-L; thick curve: FENE.

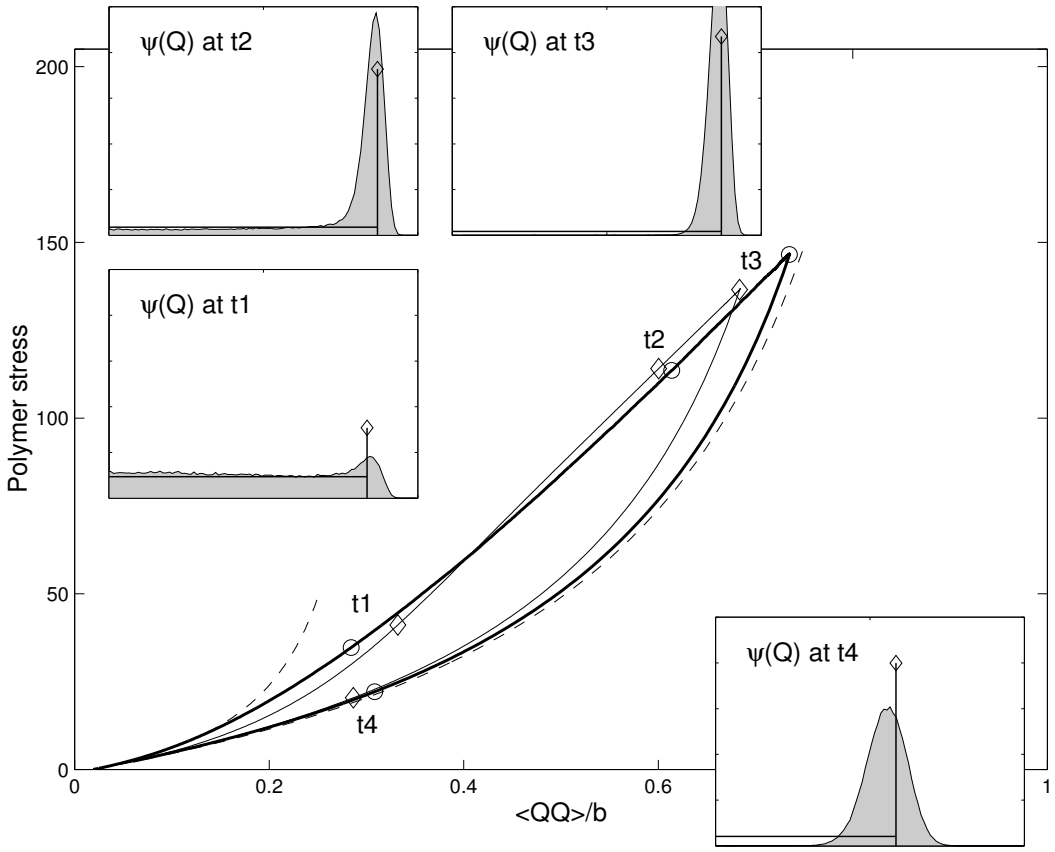

Figure 14: Startup of elongation followed by relaxation: polymer stress versus mean square extension ($b = 50$ and $k = 2$). Dashed curve (left): FENE-P^2; dashed curve (right): FENE-P; thin curve: FENE-L; thick curve: FENE. Comparison between FENE and FENE-L distribution functions at four selected times, also defined in Fig. 13. The symbols $\diamond$ and $\circ$ mark these times on the FENE-L and FENE hystereses, respectively.

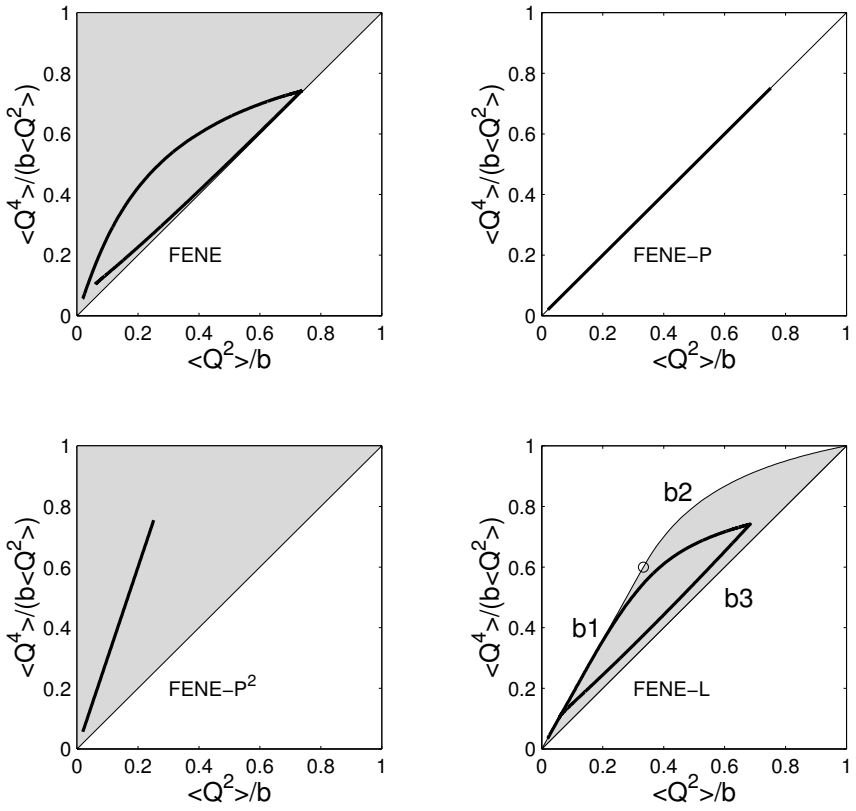

Figure 15: Startup of elongation followed by relaxation ($b = 50$ and $k = 2$): evolution of fourth moment versus second moment for FENE-P, FENE-P^2, FENE-L and FENE models (thick curves) with their admissible space (gray areas). The symbol ∘ marks the junction between boundaries **b1** and **b2** of the FENE-L admissible space. The FENE and FENE-L hystereses are travelled clockwise.

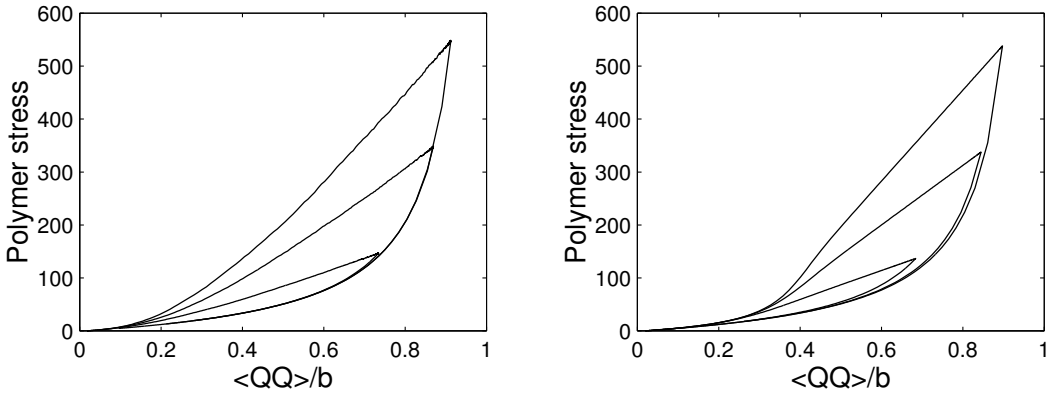

Figure 16: Startup of elongation followed by relaxation for different strain rates ($k = 2$, 4 and 6): polymer stress versus mean square extension ($b = 50$). Comparison between FENE (left) and FENE-L (right).

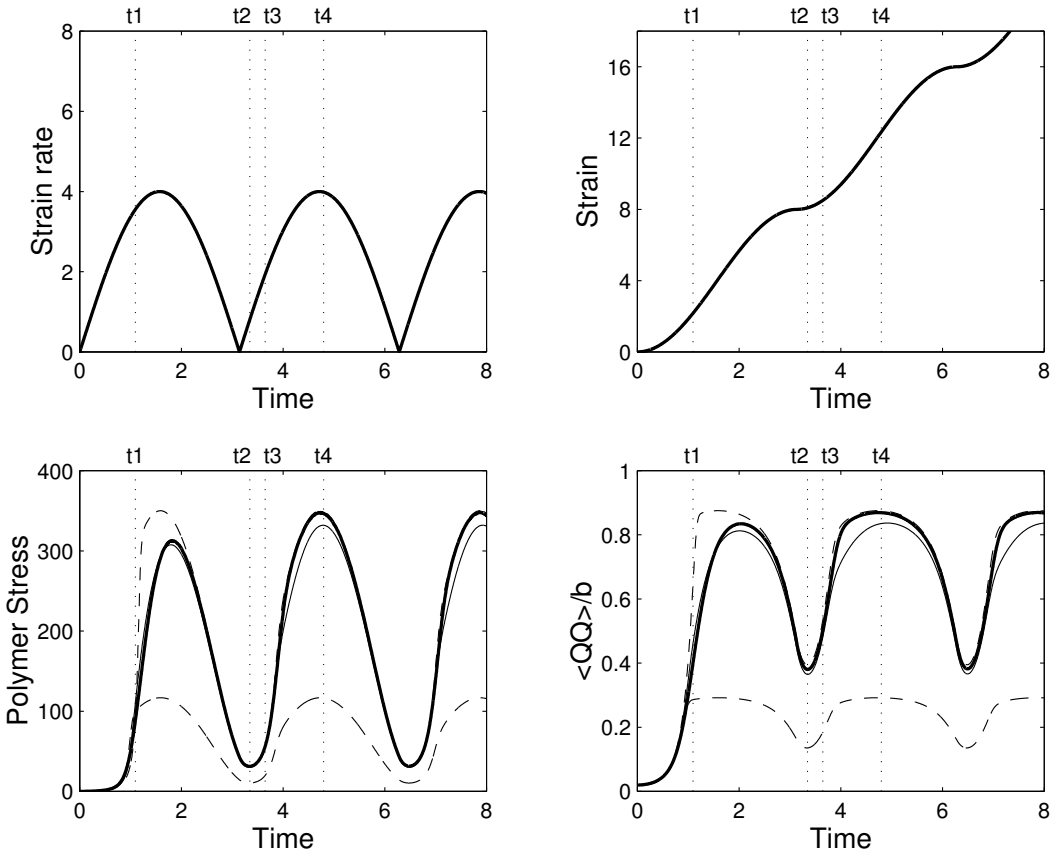

Figure 17: Periodic flow: evolution of strain rate and strain. Comparison between FENE-P, FENE-P^2, FENE-L and FENE results for the polymer stress and mean square extension ($b = 50$). Upper dashed curve: FENE-P; lower dashed curve: FENE-P^2; thin curve: FENE-L; thick curve: FENE.

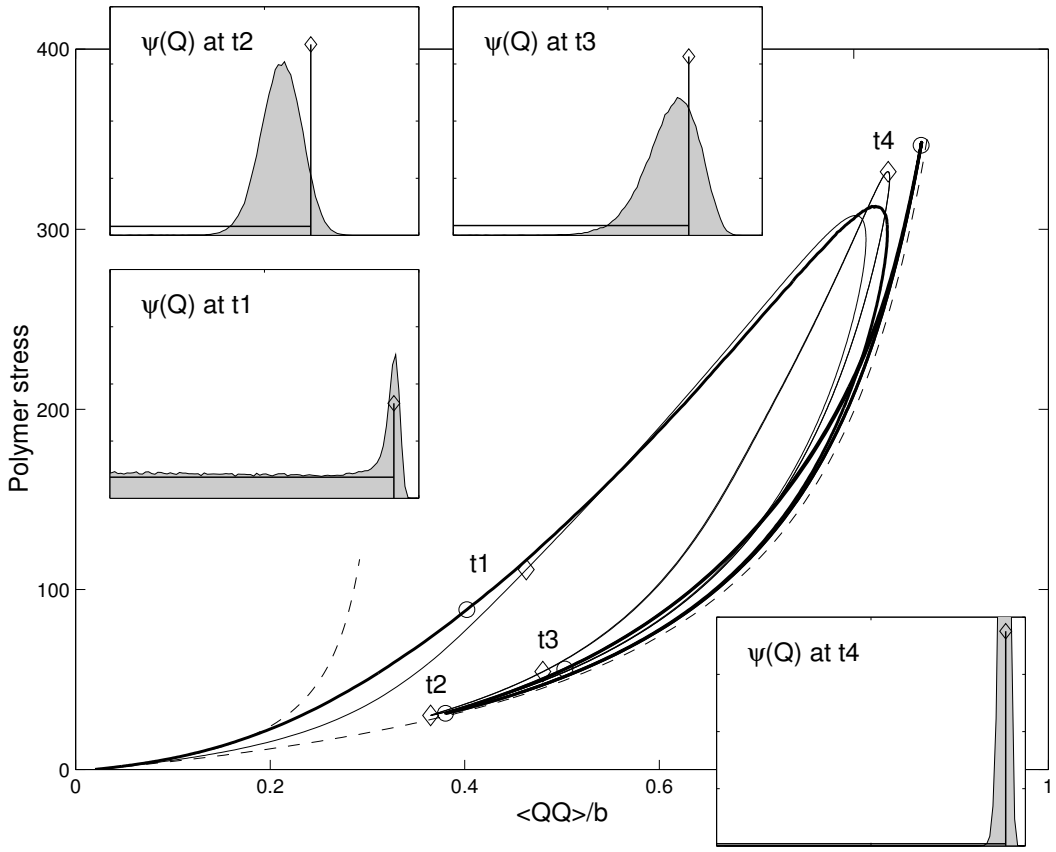

Figure 18: Periodic flow : polymer stress versus mean square extension ($b = 50$). Dashed curve (left): FENE-P^2; dashed curve (right): FENE-P; thin curve: FENE-L; thick curve: FENE. Comparison between FENE and FENE-L distribution functions at four selected times, also defined in Fig. 17. The symbols $\diamond$ and $\circ$ mark these times on the FENE-L and FENE hystereses, respectively.

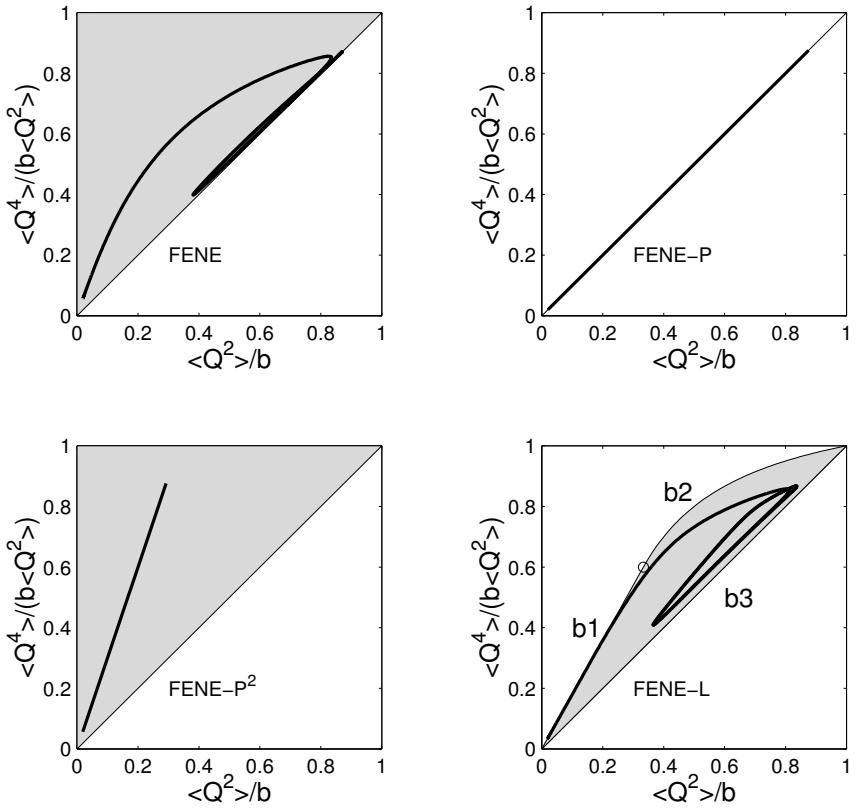

Figure 19: Periodic flow: evolution of fourth moment versus second moment for FENE-P, FENE-P^2, FENE-L and FENE models (thick curves) with their admissible space (gray areas). The symbol ∘ marks the junction between boundaries **b1** and **b2** of the FENE-L admissible space. The FENE and FENE-L hystereses are travelled clockwise.

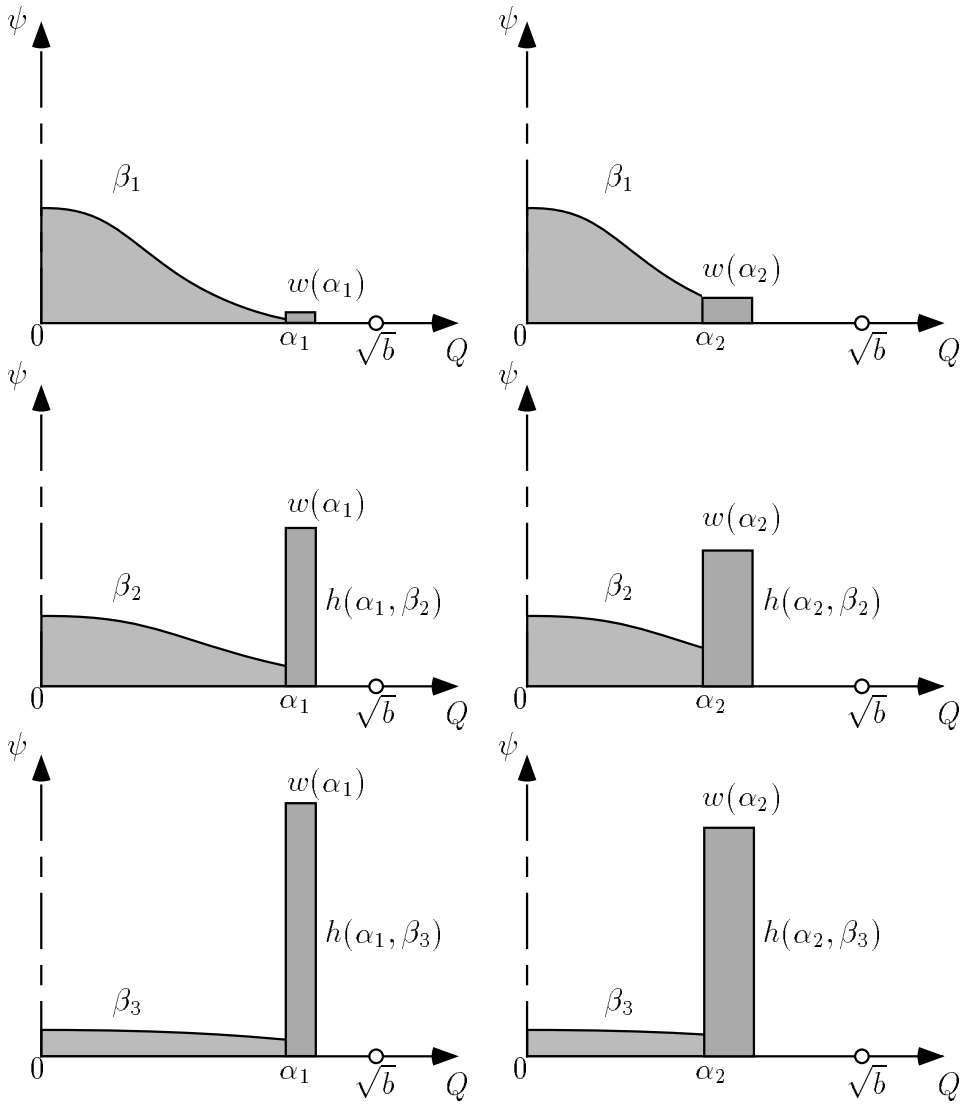

Figure 20: Proposal for an improved second-order closure: canonical distribution function (48) for different values of the parameters α and β ($\alpha_1 > \alpha_2$, $\beta_1 < \beta_2 < \beta_3$).